Contributions to Mineralogy and Petrology (2021) 176:105
https://doi.org/10.1007/s00410-021-01858-6

ORIGINAL PAPER

Measuring in situ CO_2 and H_2O in apatite via ATR-FTIR

Johannes Hammerli[1,2] · Jörg Hermann[2] · Peter Tollan[3] · Fabian Naab[4]

Received: 13 May 2021 / Accepted: 24 October 2021 / Published online: 26 November 2021
© The Author(s) 2021

Abstract

We present a new approach to determine in situ CO_2 and H_2O concentrations in apatite via attenuated total reflection Fourier transform infrared spectroscopy (ATR-FTIR). Absolute carbon and hydrogen measurements by nuclear reaction analysis (NRA) and elastic recoil detection (ERD) are used to calibrate ATR-FTIR spectra of CO_2 and H_2O in apatite. We show that CO_2 and H_2O contents in apatite can be determined via linear equations ($r^2 > 0.99$) using the integrated area of CO_2 and H_2O IR absorption bands. The main benefits of this new approach are that ATR-FTIR analyses are non-destructive and can be conducted on polished sample material surfaces with a spatial resolution of ~ 35 µm. Furthermore, the wavenumber of the phosphate IR absorption band can be used to determine the crystallographic orientation of apatite, which allows for accurate quantification of CO_2 and H_2O in randomly orientated apatite grains. The limit of quantification of H_2O in apatite is ~ 400 ppm and ~ 100 ppm for CO_2. Via two examples, one from a carbonatite and one from a metasedimentary rock, we show that this new technique opens up new possibilities for determining volatile concentrations and behavior in a wide range of hydrothermal, igneous, and metamorphic systems.

Keywords CO_2 in apatite · Absolute H_2O and CO_2 quantification in apatite · ATR-FTIR analysis of apatite

Introduction

Volatiles, especially CO_2 and H_2O, are key agents for igneous and metamorphic processes that impact the Earth's atmosphere and climate over millions of years. For example, they affect mineral stability and metamorphic reactions, and are, therefore, directly and indirectly controlling mass transfer (e.g., Phillips and Evans 2004; Williams-Jones and Heinrich 2005; Berkesi et al. 2012) as well as the melting and differentiation of the Earth's crust (e.g., Rubatto et al. 2009; see Weinberg and Hasalova 2015 for a review). However, given the fugitive behavior of CO_2 and H_2O, measuring and quantifying these components in igneous, hydrothermal, and metamorphic systems is challenging. Nevertheless, due to the critical importance in global cycling of CO_2 and H_2O for the evolution of the Earth and its climate, developing new techniques for tracing the geological distribution of these volatile components is essential (e.g., Kerrick and Caldeira 1998; Stewart and Ague 2018; Capriole et al. 2020). While fluid inclusions can provide useful insights into (Paleo)-fluid compositions (e.g., Diamond 2001), their complexity is often a limiting factor for meaningful interpretations, and doubt has been cast over the preservation and reliability of (CO_2-rich) fluid inclusions from high-grade metamorphic rocks for reconstructing fluid properties of the deep crust (e.g., Carvalho et al. 2020). An alternative approach to studying the role and presence of CO_2 and H_2O in metamorphic, igneous, and hydrothermal systems is using minerals that incorporate CO_2 and H_2O during their formation. While H_2O is readily incorporated as a major or a trace component in many common igneous and metamorphic minerals, very few of them can incorporate both of these volatile components in their crystal structure to easily-detectable concentrations (well above the ppm level).

Communicated by Timm John.

✉ Johannes Hammerli
johannes.hammerli@my.jcu.edu.au

[1] School of the Environment, Washington State University, Pullman, WA 99163, USA

[2] Institute of Geological Sciences, University of Bern, Baltzerstrasse 1+3, 3012 Bern, Switzerland

[3] Department of Earth Sciences, ETH Zürich, Clausiustrasse 25, 8092 Zurich, Switzerland

[4] Department of Nuclear Engineering and Radiological Sciences, University of Michigan, Ann Arbor, MI 48109, USA

Apatite ($Ca_5(PO_4)_3(F,Cl,OH)$), is a ubiquitously present accessory phase in terrestrial and extra-terrestrial rocks that is able to incorporate significant amounts of H_2O and CO_2, reaching weight % concentrations of either component (Binder and Troll 1989; Santos and Clayton 1995; Boyce et al. 2010; Li et al. 2020; Pan and Fleet 2002 for a review). Note that despite C being incorporated in apatite in the form of carbonate (CO_3^{2-}) and H as OH^-, we follow the conventional reporting of C and H concentrations in their oxide component as CO_2 and H_2O that would be released upon heating of apatite. Apatite has the general formula $M_5(ZO_4)_3X$, with H_2O and CO_2 hosted in different crystallographic locations. Typically, the M site is mainly filled by Ca^{2+} but can accommodate significant amounts of divalent Sr^{2+}, as well as Ba^{2+}, Pb^{2+}, light rare earth elements (REEs), and also Na^+. The Z site is mainly dominated by P^{5+}, however, As^{5+}, Si^{4+}, C^{4+}, and S^{6+} can also be present in considerable quantities. F^-, OH^-, Cl^-, and CO_3^{2-} share the channel anion X site (Pan and Fleet 2002 and references therein). The H_2O content of apatite has been used in the past (e.g., Zhu and Sverjensky 1991) to estimate H_2O contents in fluids and melts (Stock et al. 2018; Popa et al. 2021) and recent studies have also aimed at using CO_2 contents of apatite to gain insight into CO_2 contents of igneous systems (Riker et al. 2018).

One of the overarching goals of accurately measuring CO_2 and H_2O in apatite is to determine partition coefficients of CO_2 and H_2O between apatite, aqueous fluids, and melts to calculate CO_2 and H_2O contents in igneous, hydrothermal, and metamorphic systems. One of the challenges for realizing this goal is the accurate, routine measurement of CO_2 and H_2O on a (sub-) grain scale. For example, the H_2O content of apatite is typically estimated via stoichiometric calculations based on electron probe microanalysis (EPMA) measurements (e.g., Deer et al. 2013; Ketcham 2015) but meaningful calculation of H_2O in apatite in this way is notoriously problematic. One of the reasons is that the accurate quantification of Cl, and especially F, is difficult (Stormer et al. 1993; Goldoff et al. 2012; Stock et al. 2018), yet paramount, since Cl, F, and OH share the same site in apatite crystals. Other, less routine, in situ methods, such as secondary ionization mass spectrometry (SIMS) have also been employed for absolute H_2O quantification in apatite with a high spatial resolution (Barnes et al. 2014; Hu et al. 2015). A recent comparison of H_2O contents measured by SIMS with H_2O concentrations determined stoichiometrically based on EPMA measurements illustrates the challenge of accurately determining H_2O, as the two methods produced H_2O values differing by a factor of two in some cases (Riker et al. 2018). Furthermore, the incorporation of CO_2 at the same (anion) site (see above) further complicates accurate H_2O constraints via stoichiometric approaches. While the presence of CO_2 in natural apatite has been recognized for some time (e.g., Gulbrandsen et al. 1966; Elliott 1994; Fleet et al. 2004; Deer et al. 2013 and references therein), the quantitative (in situ) measurement of CO_2 remains difficult despite recent developments to quantify CO_2 contents in apatite via SIMS (Riker et al. 2018; Li et al. 2020). In addition to SIMS, one promising avenue for CO_2 and H_2O detection and quantification in apatite on a sub-grain level is transmission Fourier transform infrared spectroscopy (FTIR) on sample wafers polished on both sides (e.g., Tacker 2004, 2008). Recent work by Wang et al. (2011) and Clark et al. (2016) have shown that in situ transmission FTIR measurements and the resulting spectra can be calibrated and used for absolute H_2O and CO_2 quantification down to ppm levels in individual apatite grains. However, for the in situ transmission FTIR method, samples need to be prepared as doubled-sided polished wafers, which can be challenging for minute grains (< 200 µm), which is the most common form of apatite occurrence in crustal rocks.

In this study, we explore the potential of in situ attenuated total reflection (ATR)-FTIR analyses of polished apatite grains (i.e., in polished thin sections or grain mounts) to determine absolute H_2O and CO_2 concentrations. We have calibrated the ATR-FTIR method for measuring H_2O and CO_2 concentrations in apatite minerals with absolute hydrogen and carbon concentrations determined by elastic recoil detection (ERD) and nuclear reaction analysis (NRA). Crucially, the ATR-FTIR technique does not require double polishing and hence has the potential to be applied to a far greater array of natural apatites. Our data, produced by ATR-FTIR, show that H_2O and CO_2 contents in apatite as low as ~ 400 ppm and ~ 100 ppm, respectively, can be quantified accurately. Furthermore, based on FTIR spectra we show that the crystallographic orientation of apatite can be resolved, which is critical for accurate H_2O and CO_2 quantification in randomly orientated apatite grains. Our study presents a new, effective and broadly applicable approach to accurately measure CO_2 and H_2O in apatite via ATR-FTIR, contributing to the further development of using CO_2 and H_2O concentrations in apatite as a tool to estimate the concentration of these volatiles in igneous, hydrothermal, and metamorphic systems.

Sample material and preparation

A total of eight apatite specimens, most of them between 1 and 2 cm in length, were used to develop the analytical technique for CO_2 and H_2O quantification by ATR-FTIR. Samples used in this study include apatite from the High Atlas Mountains (HAM), Morocco, purchased from an online vendor and apatite from the Mud Tank (MT) carbonatite, Northern Territory, Australia, collected by J. Hermann. We also used apatite from Hormuz Island (HRZ), Iran (NMBE B6634), procured from the Natural History

Museum Bern, Switzerland (NMBE) and apatite crystals named "SAP3" and "VOH", both originating from Madagascar. However, while VOH (NMBE 40865) originates from Milanoa in the Vohémar province and was provided by the NMBE, the exact location of SAP3 is unknown as it was purchased from an online vendor (see also Hammerli et al. 2021). Apatite specimen "GL", which comes from a large apatite crystal from a carbonatitic vein in Greenland, was obtained from K. Thrane of the Geological Survey of Denmark and Greenland. "YAM" apatite is a euhedral apatite embedded in a pink calcite matrix from the Yates Mine, Otter Lake, Canada. A smaller grain (~5 mm) "HOI" from the Hohe Ilmen mountains near Miass, Russia, provided by the NMBE, was also used for method development, however, the crystal chip was too small for Nuclear Reaction Analysis (NRA) or Elastic Recoil Detection (ERD) analyses.

NRA required the preparation of sample wafers (~4 mm × 4 mm), which were polished stepwise from 6 to 0.5 µm with diamond paste on both sides. Larger sample wafers (~8 mm × 5 mm) were prepared for ERD analyses following the same procedure as for NRA. For ATR-FTIR analyses, apatite specimens with euhedral crystal habits were cut parallel and perpendicular to the optical c-axis, embedded in 1-inch epoxy mounts, and subsequently stepwise polished from 6 to 1 µm with diamond paste. For each sample, randomly orientated pieces of the same wafers prepared for NRA and ERD analyses were embedded in epoxy to check sample homogeneity and to assess crystallographic effects on ATR-FTIR analyses.

Methods

Nuclear reaction analysis

NRA via the 1.7 MV tandem accelerator at the Michigan Ion Beam Laboratory (MIBL) of the University of Michigan was used to determine absolute carbon concentrations in apatite (Mathez et al. 1987; Proust et al. 1994; Cherniak et al. 2010; Clark et al. 2016). A high-energy beam (1.4 MeV) of deuteron (^{2}H) particles was used to bombard the polished apatite surface to activate the ^{12}C (d,p) ^{13}C nuclear reaction ($^{12}C + {}^{2}H \rightarrow {}^{13}C + {}^{1}H$, Proust et al. 1994; Wang and Nastasi 2009; Csedreki et al. 2014). As the deuteron beam interacts with the sample, ^{2}H particles react with the target nucleus of carbon (^{12}C), converting the target nucleus to a new nucleus (^{13}C), while releasing ^{1}H as a reaction product with a specific amount of energy. The liberated ^{1}H ions are subsequently detected in the Si charged-particle detector, set at a scattering angle of 160° with a 15 keV energy resolution. No filter foil was used in front of the detector; thus, the same detector detected the Rutherford Backscattered deuterons and the products of the nuclear reaction. The estimated sampling depth is ~6 µm as determined by the SIMNRA software (Mayer 1999). The SIMNRA program was also used for NRA spectrum modeling to determine absolute atomic carbon concentration. Being an absolute method, no independent calibration is necessary for NRA, however, we verified the procedure by analyzing a calcite ($CaCO_3$). The obtained carbon concentration of 19.3 ± 1.3 at.%, agrees with the stoichiometric concentration of carbon (20 at.%) in calcite.

Elastic recoil detection

All ERD measurements were carried out at the Michigan Ion Beam Laboratory (University of Michigan). We used the 1.7 MV tandem accelerator with a similar setup as discussed in previous studies (Aubaud et al. 2009; Bureau et al. 2009; Wang et al. 2011). A 2.5 MeV He++ ion beam was used to impact the polished apatite surface from which H ions are released. This beam energy permits the analysis of the H content in the sample to a depth of ~500 nm, while two detectors simultaneously collect the ERD and Rutherford back-scattering (RBS) spectra. The number of particle incidents on the sample during the acquisition of the ERD spectrum was measured via the RBS spectrum. A 12.5 µm Kapton film was used in front of the ERD detector to filter out ions heavier than H. Also, a Kapton polyimide ($H_{10}C_{22}N_2O_5$) foil was used as the H standard to determine the ERD detector solid angle relative to the RBS detector solid angle (Wang 2004). No standards or additional calibration are required to determine absolute H concentration via the ERD method (Tirira et al. 1991; Aubaud et al. 2009; Bureau et al. 2009). Atomic H concentrations in the apatite samples were determined via ERD and RBS spectrum modeling using the SIMNRA program (Mayer 1999).

EPMA

Concentrations of the major elements Ca, P, Si, F, and Cl, as well as the minor element contents (Mn, Mg, Fe, Na, S) in the apatite samples were obtained via EPMA using a JEOL JXA 8200 superprobe housed at the Institute of Geological Sciences, University of Bern, Switzerland. The analytical potential was set at 15 kV and 4 nA beam current. The beam diameter was set at 15 µm and counting times were 20 s on peak and 10 s on background for each element, besides for S, which was counted for 30 s on peak and 60 s on background. Na, F, Ca, and Cl were measured first, followed by the other elements. All apatite grains were measured perpendicular to their c-axis as suggested by Goldoff et al. (2012) to avoid time-dependent X-ray intensity variations of F and Cl. The data were processed using ZAF corrections and standardized

via in-house standards (apatite for P_2O_5 and CaO, magnetite for FeO, celestine for SO_3, topaz for F, orthoclase for SiO_2, tugtupite for Cl, forsterite for Mg, albite for Na, and spessartine for MnO). The stoichiometry of the unknowns was calculated following the method of Ketchman (2015).

FTIR

We used a Bruker Tensor II spectrometer coupled to a Bruker Hyperion 3000 microscope housed at the Institute of Geological Sciences, University of Bern, to acquire FTIR spectra. The setup includes a fully automated sample stage and a dry air-purged analytical chamber to minimize atmospheric interferences. FTIR spectra of apatite were acquired using an ATR objective coupled with a single-spot mercury cadmium telluride (MCT) detector. The objective is composed of a germanium (Ge) two-reflection ATR element with internal and external incidence angles of 21.5° and 37°, which is placed in contact with the sample surface. The infrared light, emitted from a SiC globar source, is internally-reflected through the Ge crystal resulting in the generation of an evanescent wave which transmits into the uppermost portion of the sample (spot diameter of ~ 35 µm). The penetration depth of the evanescent wave is wavenumber- and incident angle-dependent, but is < 1 µm for the wavenumbers of interest in this study. Spectra were acquired using unpolarized light, 128 scans and a wavenumber resolution of 4 cm^{-1}. The pressure of the Ge crystal was set at 2, which corresponds to 2.6 N of force. A background measurement of (dry-purged) air was collected before each measurement. Subsequently, the spectra of the unknown were baseline corrected using the concave rubber band algorithm of OPUS® with 64 points and three iterations. The area of the bands in the spectra representing the absorption of the "H_2O" and "CO_2" vibration bands in the wavenumber regions 3600 cm^{-1} to 3400 cm^{-1} and 1600 cm^{-1} to 1300 cm^{-1}, respectively, were integrated using the OPUS® program. Since the CO_2 and H_2O absorption bands in apatite can be located at slightly different wavenumbers, a separate integration window was defined for each sample. The band areas were then used to calibrate the FTIR signal to absolute CO_2 and H_2O contents of apatite (see below).

Results

NRA and ERD data

Nuclear reaction analyses of the five apatite specimens (HAM, MT, SAP3, YAM, and GL) were performed on both sides of each wafer and the obtained C contents (in at.%) range from ~ 0.07 to ~ 0.62, which translates to mean CO_2 wt% values of 0.14 ± 0.03 (2SD) for HAM, 0.39 ± 0.03 (2SD) for MT, 0.46 ± 0.06 (2SD) for SAP3, 1.05 ± 0.28 (2SD) for YAM, and 1.12 ± 0.18 (2SD) for GL (Table 1).

Table 1 NRA and ERD data of apatite specimens MT, SAP3, GL, YAM, HAM, VOH, and HRZ

Sample	MT	SAP3	GL	YAM	HAM	VOH	HRZ
C (at.%)	0.21	0.23	0.55	0.60	0.07		
	0.20	0.25	0.62	0.50	0.08		
CO_2 (wt%)	0.40	0.44	1.05	1.15	0.13		
	0.38	0.48	1.18	0.95	0.15		
Mean CO_2 (wt%)	0.39 ± 0.03	0.46 ± 0.06	1.12 ± 0.18	1.05 ± 0.28	0.14 ± 0.03		
H (at.%)	2.68					2.49	0.58
	3.05					2.60	0.60
	2.50						
	2.90						
	2.58						
	2.90						
H_2O (wt%)	1.02					0.96	0.22
	1.16					1.01	0.23
	0.95						
	1.10						
	0.98						
	1.14						
Mean H_2O (wt%)	1.06 ± 0.17					0.99 ± 0.06	0.23 ± 0.01

Carbon and hydrogen contents of the above apatite specimens are reported as C at.% and H at.% with their corresponding CO_2 and H_2O concentrations in wt%. Uncertainties are 2SD

Table 2 Mean values of EPMA measurements of apatite

Sample	YAM		GL		HAM		MT		VOH		SAP3		HRZ		HOI		19JH-03	
	Mean	2SD	Mean	2SD	Mean	2SD	Mean	2SD	Mean	2SD	Mean	2SD	Mean	2SD	Mean	2SD	Mean	2SD
wt%	(*n* = 6)	±	(*n* = 4)	±	(*n* = 7)	±	(*n* = 5)	±	(*n* = 7)	±	(*n* = 11)	±	(*n* = 4)	±	(*n* = 5)	±	(*n* = 5)	±
CaO	54.87	0.62	54.08	0.58	55.38	1.49	55.71	0.37	54.83	1.02	55.95	0.30	52.99	0.53	54.59	0.52	56.23	0.55
P_2O_5	39.30	0.56	41.37	1.02	41.21	0.87	42.12	1.10	42.17	0.89	39.88	1.56	39.04	0.76	40.98	1.00	42.58	0.39
SiO_2	0.91	0.12	0.02	0.04	0.43	0.16	< 0.01	0.02	0.02	0.05	0.72	0.06	0.37	0.10	< 0.01	< 0.01	0.02	0.03
SO_3	0.50	0.06	0.11	0.01	0.32	0.14	0.01	0.03	0.04	0.05	0.63	0.05	0.05	0.02	0.07	0.03	< 0.01	< 0.01
Na_2O	0.07	0.04	0.56	0.07	0.05	0.06	0.19	0.10	0.02	0.04	0.05	0.06	0.56	0.18	0.20	0.06	0.02	0.04
MgO	0.01	0.03	0.05	0.04	0.01	0.04	0.06	0.03	0.03	0.04	0.01	0.02	0.06	0.02	0.01	0.03	< 0.01	< 0.01
FeO	0.02	0.06	0.15	0.12	0.04	0.06	0.08	0.03	0.06	0.05	0.03	0.06	0.04	0.06	0.04	0.09	0.02	0.03
MnO	0.02	0.04	0.04	0.06	0.02	0.05	0.02	0.05	0.08	0.05	0.01	0.03	< 0.01	< 0.01	0.11	0.05	0.04	0.04
F	3.94	0.25	2.28	0.23	2.13	0.23	1.81	0.14	1.80	0.17	3.59	0.35	3.04	0.23	3.79	0.13	3.12	0.16
Cl	0.04	0.04	0.07	0.04	0.54	0.06	0.04	0.03	0.07	0.03	0.15	0.02	0.55	0.05	< 0.01	0.01	< 0.01	< 0.01
CO_2*	1.03	0.07	1.11	0.08	0.13	0.01	0.39	0.03			0.48	0.03			0.54	0.03	0.02	0.03
Total	100.91	0.67	100.09	0.34	101.25	0.44	100.00	0.58	99.96	0.95	100.96	1.10	98.47	0.19	98.40	0.25	102.04	0.74
Calc. OH			0.88	0.25	1.15	0.22	1.62	0.16	1.71	0.18			0.21	0.22			0.61	0.14
Total**	98.46	1.13	99.75	1.26	100.38	1.43	101.29	1.52	100.06	1.19	99.83	1.51	95.51	1.42	98.47	1.00	101.36	0.78
APFU																		
Ca	9.94	0.08	9.68	0.15	9.98	0.24	9.93	0.13	9.90	0.19	10.09	0.24	10.07	0.08	9.95	0.17	10.00	0.07
P	5.63	0.03	5.85	0.07	5.87	0.11	5.93	0.05	6.02	0.08	5.68	0.11	5.86	0.03	5.88	0.07	5.99	0.03
Si	0.15	0.02	< 0.01	0.01	0.07	0.03	< 0.01	< 0.01	< 0.01	0.01	0.12	0.01	0.07	0.02	< 0.01	< 0.01	< 0.01	< 0.01
S	0.06	0.01	0.01	< 0.01	0.04	0.02	0.00	0.00	0.01	0.01	0.08	0.01	0.01	< 0.01	0.01	< 0.01	< 0.01	< 0.01
Na	0.02	0.01	0.18	0.02	0.02	0.02	0.06	0.03	0.01	0.01	0.02	0.02	0.19	0.06	0.07	0.02	< 0.01	< 0.01
Mg	< 0.01	0.01	0.01	0.01	< 0.01	0.01	0.02	0.01	0.01	0.01	< 0.01	0.01	0.02	< 0.01	< 0.01	0.01	< 0.01	< 0.01
Fe	< 0.01	0.01	0.02	0.02	0.01	0.01	0.01	< 0.01	0.01	0.01	< 0.01	0.01	0.01	0.01	< 0.01	0.01	< 0.01	< 0.01
Mn	< 0.01	0.01	0.01	0.01	< 0.01	0.01	< 0.01	0.01	0.01	0.01	< 0.01	0.01	< 0.01	< 0.01	0.02	0.01	< 0.01	< 0.01
F	2.11	0.15	1.20	0.14	1.13	0.12	0.95	0.08	0.96	0.09	1.91	0.21	1.71	0.14	2.03	0.07	1.64	0.08
Cl	0.01	0.01	0.02	0.01	0.15	0.02	0.01	0.01	0.02	0.01	0.04	0.01	0.17	0.01	< 0.01	< 0.01	< 0.01	< 0.01
C	0.24	< 0.01	0.25	< 0.01	0.03	< 0.01	0.09	< 0.01	< 0.01	< 0.01	0.11	< 0.01	< 0.01	< 0.01	0.13	< 0.01	< 0.01	< 0.01
OH		0.12	0.65	0.09	0.70	0.17	1.02	0.06	0.99	0.13	0.06	0.15	0.19	0.13		0.07	0.37	0.12
C on P site	0.16	0.03	0.13	0.06	0.02	0.09	0.07	0.05			0.12	0.10			0.11	0.07	0.01	0.03
C on OH site	0.08	0.03	0.12	0.06	0.01	0.09	0.02	0.05			< 0.01	0.10			0.02	0.06	< 0.01	< 0.01

Uncertainties are show as the 2SD of the performed analyses of each sample. The stoichiometries are calculated following the method of Ketcham (2015). The OH content was calculated assuming that the anion site is filled with F, Cl, OH, and CO_2 and that the Z-site consisting of P, Si, S, and C, is 6 APFU. The CO_2* contents of samples YAM, GL, HAM, MT, and SAP3 were determined by NRA. CO_2 in HOI and 19-JH-03 apatite was measured by FTIR. See main text and Fig. 12 for a comparison between stoichiometric OH calculations and ATR-FTIR measurements

*Determined by NRA and FTIR (HOI)

**Corrected for Cl–O and F–O

All analyses of the individual apatite specimens are within their analytical uncertainty, which is estimated at ~ 10%.

Elastic recoil detection analyses were performed on the apatite specimens for which a H_2O signal was detected by ATR-FTIR and a large enough sample material was available (8 mm × 5 mm). The front- and back-side of three MT apatite wafers were analyzed and the resulting H contents range from ~ 2.5 to 3.1 at.%, which means that all analyses are within the analytical uncertainty of ~ 10%. The resulting mean H_2O concentration in MT apatite is 1.06 ± 0.17 wt% (2SD). VOH apatite returned H at.% contents of 2.49 and 2.60, which is the equivalent of 0.96 and 1.01 wt% H_2O and a mean of 0.99 ± 0.06 (2SD). The two ERD measurements of HRZ apatite returned H at.% values of 0.58 and 0.60, which equals a mean of 0.23 ± 0.01 wt% H_2O (2SD) (Table 1).

Electron probe microanalysis (EPMA)

The composition of the eight apatite specimens used for the method development are given in Table 2. Their stoichiometries were calculated following the method by Ketcham (2015), based on 25 oxygens. CaO contents of the measured specimens range from ~ 54.8 to 56.1 wt% and P_2O_5 contents vary from ~ 40.3 to 42.3 wt%. Fluorine is the most important anion in all the analyzed specimens, ranging from ~ 1.80 to ~ 3.94 wt%, while chlorine contents vary between ~ 0.04 and 0.55 wt%. MnO and MgO contents are ≤ 0.11 wt% in all measured samples and the highest FeO was found in the GL apatite with ~ 0.15 wt%. GL apatite also contains the highest SiO_2 concentration at ~ 0.91 wt%, while SAP3 apatite contains the most SO_3 (~ 0.63 wt%). In addition to elevated Cl contents (~ 0.55 wt%), HRZ also contains ~ 0.56 wt% Na_2O, which is, together with GL apatite, the highest concentration of all analyzed apatite specimens (Table 2). Using the above concentrations, stoichiometric calculations, which also consider the CO_2 content on the anion site (1-C-F-Cl), reveal the highest OH concentrations in VOH and MT apatite, of ~ 1.71 and 1.62 wt%, respectively, followed by HAM (~ 1.15 wt%), GL (~ 0.88 wt%), and HRZ (~ 0.21 wt%). According to the stoichiometric constraints based on EPMA data, apatite specimens YAM, SAP3, and HOI are devoid of OH.

ATR-FTIR

IR absorption of phosphate in apatite

The phosphate (PO_4) absorption band in apatite is typically located at wavenumbers around ~ 1000 cm^{-1} (e.g., Regnier et al. 1994) and is the most intense (i.e., highest) signal in the spectra (Fig. 1). ATR-FTIR measurements of the apatite specimens in this study typically produce absorption PO_4 bands between the wavenumbers ~ 1022 cm^{-1} and ~ 1013 cm^{-1}. Lower wavenumber absorption bands for PO_4 (e.g., 1013 cm^{-1} bands) are produced by analyzing apatite perpendicular to the c-axis (red section in Fig. 2), whereas a rotation of the apatite crystal leads to a shift of

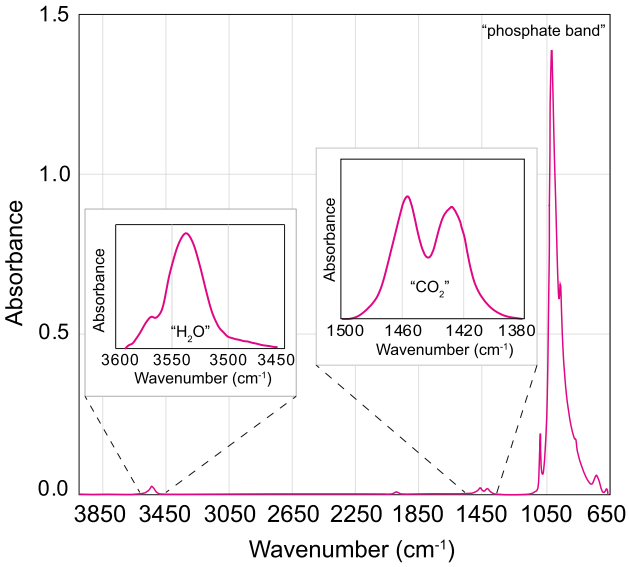

Fig. 1 Background-corrected non-polarized ATR-FTIR spectrum of apatite shows phosphate, CO_2, and H_2O absorption band

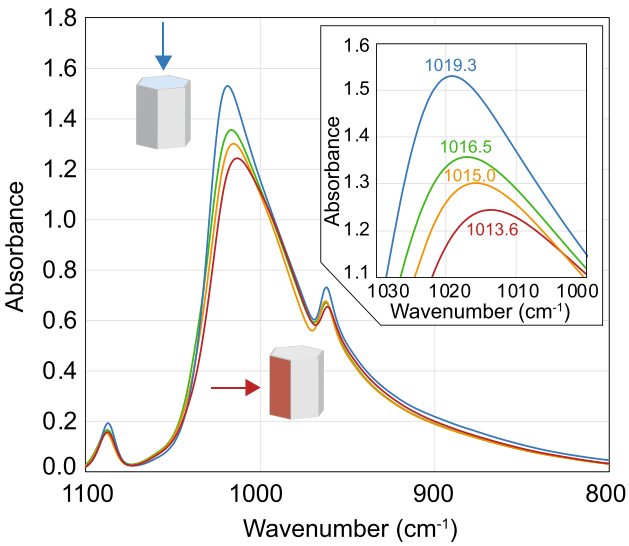

Fig. 2 Phosphate non-polarized IR absorption bands of apatite when measured along different crystallographic orientations. Blue absorption band represents ATR-FTIR analysis parallel to the c-axis and red absorption band shows phosphate absorption when measured perpendicular to the c-axis of the apatite crystal. Measurements in between the two extreme crystallographic orientations are shown in green and orange. The inset shows the wavenumber shift of the phosphate absorption band from 1019.3 cm^{-1} when measured (parallel) along the c-axis to 1013.3 cm^{-1} for measurements perpendicular to the c-axis. (For interpretation of the references to color in this figure legend, the reader is referred to the web version of this article.)

the PO_4 absorption peak to higher wavenumbers (blue section; Fig. 2). Please note that we use the terms "parallel to c-axis" and "perpendicular to c-axis" as the orientation of the crystal with respect to the ATR alignment. ATR measurements are all done using unpolarized light and thus this notation does not refer to a polarized absorbance of apatite as might be used in polarized transmission measurements. To avoid confusion, all measurement directions are indicated in the figures. Consequently, a PO_4 band shift of ~ 6 to 8 cm^{-1} wavenumbers to a band position of ~ 1019 cm^{-1} or 1022 cm^{-1} is typically observed when apatite is analyzed parallel to the c-axis (i.e., 90° rotation of the crystal). In some cases, the phosphate absorption band heights in the FTIR spectra are positively correlated with the band wavenumbers (Fig. 2). However, this is not universally the case and appears to depend on the individual apatite specimen. Further investigation is required to determine if there is a link between the phosphate absorption band height, the crystallographic orientation, and the composition of the analyzed sample.

IR absorption of CO_2 bands in apatite

The incorporation of C in apatite results in multiple distinct bands in FTIR spectra due to a range of absorption bands caused by different vibration modes (e.g., Fleet et al. 2004, 2011; Gunaskeran et al. 2006; Tacker 2008; Clark et al. 2016). Several distinct bands in the wavenumber region between 1570 and 1360 cm^{-1} have been associated with CO_2 (CO_3^{2-}) in apatite (e.g., Comodi and Liu 2000; Fleet and Liu 2003; Fleet et al. 2004; Tacker 2008) and these absorption bands are the most promising for directly quantifying the CO_2 content of apatite due to their clear separation from other absorption bands (Fig. 1 and see Grunenwald et al. 2014; Clark et al. 2016). The CO_2 absorption bands generated by ATR-FTIR analysis are typically an order of magnitude smaller than the absorption bands of PO_4 (Fig. 1). Furthermore, similar to previous studies (e.g., Clark et al. 2016), we found that different crystallographic orientations of apatite affect the IR absorption of CO_2, which results in different CO_2 band heights in some of the studied specimens. In general, the CO_2 absorption bands in the wavenumber region from 1570 to 1360 cm^{-1} reach their maximum heights when apatite is analyzed perpendicular to its c-axis (Fig. 3). Conversely, analysis parallel to the c-axis can lead to smaller CO_2 absorption bands, which confirms the findings of previous studies (e.g., Clark et al. 2016). Accordingly, integrated CO_2 absorption band areas of analyses conducted perpendicular to the c-axis are by a factor of ~ 1.25 larger compared to CO_2 absorption band areas of analyses conducted parallel to the c-axis of apatite (Fig. 3). However, while this observation is true for apatite specimens that produce two distinct bands at wavenumbers of ~ 1455 cm^{-1} and ~ 1430 cm^{-1} (Fig. 3), for some apatite, such as specimens GL or MT, the CO_2 absorption bands do not change to the same extent in response to different crystallographic orientations (see GL and MT in Fig. 3). It is noteworthy that apatite specimens GL and MT produce broader CO_2 absorption bands compared to, for example, YAM or HOI apatite specimens, with an additional "CO_2" band between the two main absorption bands (Fig. 3). Importantly, this third band at, for example, ~ 1438 cm^{-1} in MT, increases when analyzed parallel to the crystal's c-axis. Thus, the integrated CO_2 absorption bands of such apatite samples are indistinguishable and independent of the sample's crystallographic orientation (Fig. 3).

ATR-FTIR analyses of randomly orientated fragments of apatite YAT, SAP3, and HOI show that CO_2 band heights and their corresponding integrated absorption areas do not change linearly when apatite fragments with different crystallographic orientations are analyzed (see above). Figure 4 shows that the integrated absorption band area only changes when the apatite grains are analyzed (sub) parallel to their c-axis as determined by the phosphate band shifts to wavenumbers ≤ 1019 cm^{-1}. However, the reason for this apparent "step-change" in the absorption of CO_2 has to be further explored, especially since a continuous change in the H_2O absorption is observed (see below).

IR absorbance of H_2O bands

The most prominent IR H_2O (OH) absorption bands of apatite typically produce bands at wavenumbers between ~ 3600 and 3400 cm^{-1} (Fowler 1974; Freund and Knobel 1977; Tacker 2004 and reference therein), with the major band typically located around ~ 3540 cm^{-1} (Fig. 1). Similar to the CO_2 signals, absorption band heights of H_2O acquired in the ATR-FTIR mode are one order of magnitude smaller than the main PO_4 absorption band (Fig. 1). Compared to the CO_2 absorption bands, the degree of H_2O absorption in apatite and the corresponding band height is much more dependent on the crystallographic orientation of the sample—an observation also reported in previous studies (see Wang et al. 2011; Clark et al. 2016). Unlike the CO_2 absorption bands, IR H_2O absorption in apatite changes continuously when a sample is analyzed along different crystallographic orientations (i.e., being rotated around an axis perpendicular to the c-axis). Most IR is absorbed by "H_2O" when apatite is measured parallel to the c-axis (Fig. 5A), along the channels of the crystal, where the majority of H_2O and halogens are typically located (see above). The integrated H_2O absorption area of ATR-FTIR analyses parallel to the c-axis is ~ 4 times larger than the integrated H_2O absorption area obtained from measurements perpendicular to the c-axis of apatite. This crystallographic control on the H_2O absorption leads to a linear correlation between the crystallographic

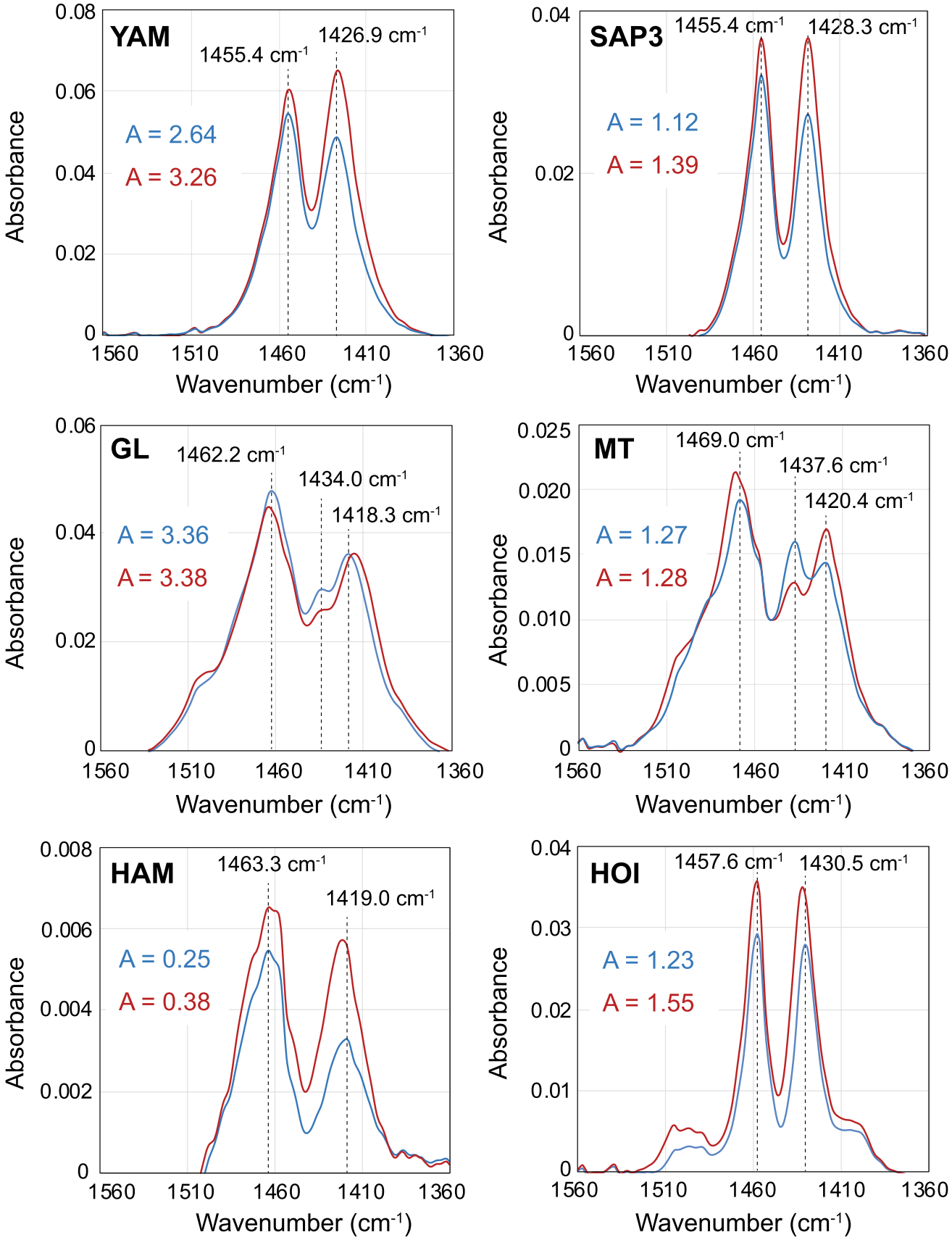
YAM
1455.4 cm-1
1426.9 cm-1
A = 2.64
A = 3.26
SAP3
1455.4 cm-1
1428.3 cm-1
A = 1.12
A = 1.39
GL
1462.2 cm-1
1434.0 cm-1
1418.3 cm-1
A = 3.36
A = 3.38
MT
1469.0 cm-1
1437.6 cm-1
1420.4 cm-1
A = 1.27
A = 1.28
HAM
1463.3 cm-1
1419.0 cm-1
A = 0.25
A = 0.38
HOI
1457.6 cm-1
1430.5 cm-1
A = 1.23
A = 1.55
Absorbance
Wavenumber (cm-1)

◂**Fig. 3** CO_2 absorption spectra of apatite specimens YAM, SAP3, GL, MT, HAM, and HOI. Blue spectra represent analyses parallel to the c-axis and red spectra show analyses perpendicular to the c-axis. Wavenumbers of the main bands are assigned to measurements parallel to the c-axis (blue spectra). The integrated area under the curves are given for both analyses parallel (blue) and perpendicular (red) to the c-axis (see main text for a detailed discussion on band positions). The intergraded absorption areas of samples YAM, SAP3, GL, MT, and HAM were used for the calibration of the FTIR (see main text). The 2SD uncertainty of the individual absorption areas is estimated to be ± 5% (see main text for more information)

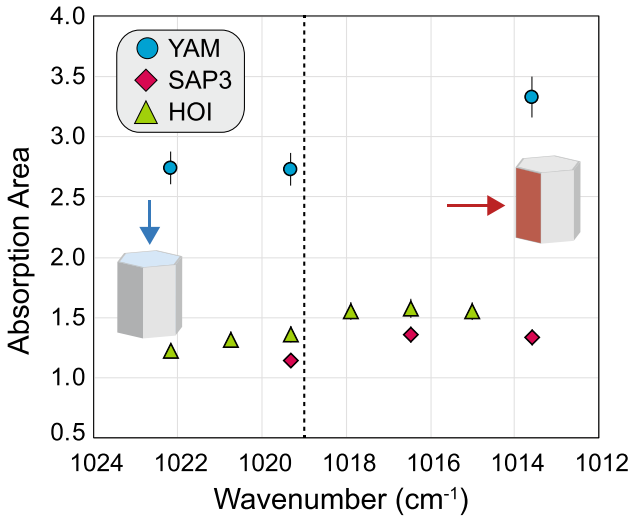

Fig. 4 Absorption area of CO_2 bands in apatite when measured on differently orientated apatite grains. Integrated absorption area of CO_2 bands (vertical axis) in apatite specimens YAM, SAP3, and HOI vs. wavenumber of the phosphate bands (horizontal axis). The highest wavenumber of the phosphate band for each sample represents analyses parallel to c-axis and the lowest wavenumbers represent analyses of apatite perpendicular to c-axis (see Fig. 2). The dotted line at wavenumber 1019 cm^{-1} marks the change of CO_2 absorption in respect to the crystallographic orientation, illustrating that lower absorption areas are obtained when the phosphate absorption band sits at ≤ 1019 cm^{-1}

orientation and the H_2O absorbance (Fig. 5B). While most of the H_2O-bearing apatite specimens contain one major H_2O absorption band in an IR spectrum, apatite specimen HRZ contains two main bands in the non-deconvoluted IR spectrum of H_2O, located at wavenumbers of ~ 3582 cm^{-1} and ~ 3470 cm^{-1} (see below).

Reproducibility and limit of quantification

To test the reproducibility of ATR-FTIR analyses of CO_2 and H_2O in apatite, we conducted repeat analyses of the same analytical spot (i.e., same location in the apatite specimen) of CO_2 and H_2O bearing apatite specimens. All spectra were acquired under the same analytical conditions and corrected identically for background noise and the same absorption band areas were integrated. Figure 6 shows 14 analyses of a YAM apatite grain (1.05 wt% CO_2) and 6 analyses of a VOH apatite grain (0.99 wt% H_2O). The standard deviation for sets of repeated CO_2 and H_2O analyses is < 2% and standard errors are < 1%. For individual measurements of sample material, we suggest to consider a conservative uncertainty of 5% for H_2O and CO_2 quantification at the 95% confidence interval.

Limit of quantification (LOQ) of ATR-FITR analyses is typically estimated as the combination of the average background signal (BG) summed with the tenfold standard deviation (SD) of the background signal. In the case of the two examples with low CO_2 and H_2O concentrations, as shown in Fig. 7, the calculated LOQ, via the above method, is similar to the approximation of LOD using signal to noise ratio (SNR), for which a ratio of 3 is typically considered as a threshold. It has to be kept in mind that the integrated absorption area is not only dependent on the absorption band height, but also on the band width. Therefore, an exact estimate of the LOQ in ppm is difficult. However, based on our data we estimate a LOQ for CO_2 of ~ 100 ppm and ~ 400 ppm for H_2O (Fig. 7). The limit of detection, constrained by the average of the BG signal summed with the threefold SD, is significantly lower and might be in the ppm range for CO_2 (Fig. 7).

Calibration of ATR-FTIR measurements to absolute CO_2 and H_2O concentrations

CO_2 calibration

We used the CO_2 contents of five apatite specimens, determined by NRA measurements (Table 1), to convert the ATR-FTIR absorbance bands to absolute CO_2 concentrations. To test the homogeneity of the apatite specimens used for the CO_2 calibration, ATR-FTIR measurements were run along transects across the different apatite specimens, orientated parallel and perpendicular to the c-axis. The integrated CO_2 absorbance bands (A) measured perpendicular to the c-axis are: 1.33 ± 0.06 (2SD) (n = 13) for MT, 1.39 ± 0.02 (2SD) (n = 24) for SAP3, 3.49 ± 0.34 (2SD) (n = 11) for GL, 3.26 ± 0.04 (2SD) (n = 19) for YAM, and 0.38 ± 0.04 (2SD) (n = 11) for HAM. Measurements parallel to the c-axis returned CO_2 absorbance band areas of 1.12 ± 0.08 (2SD) (n = 13) for SAP3 and 2.63 ± 0.15 (2SD) (n = 21) for YAM (see above). Uncertainties (2SD) of all average values are < 10%, however, for samples that show a 2SD of > 5% for their integrated CO_2 absorbance areas (e.g., SAP3) we infer that small compositional heterogeneities might exist.

For the absolute CO_2 (in wt%) determination by ATR-FTIR, we constructed two calibration lines (parallel and

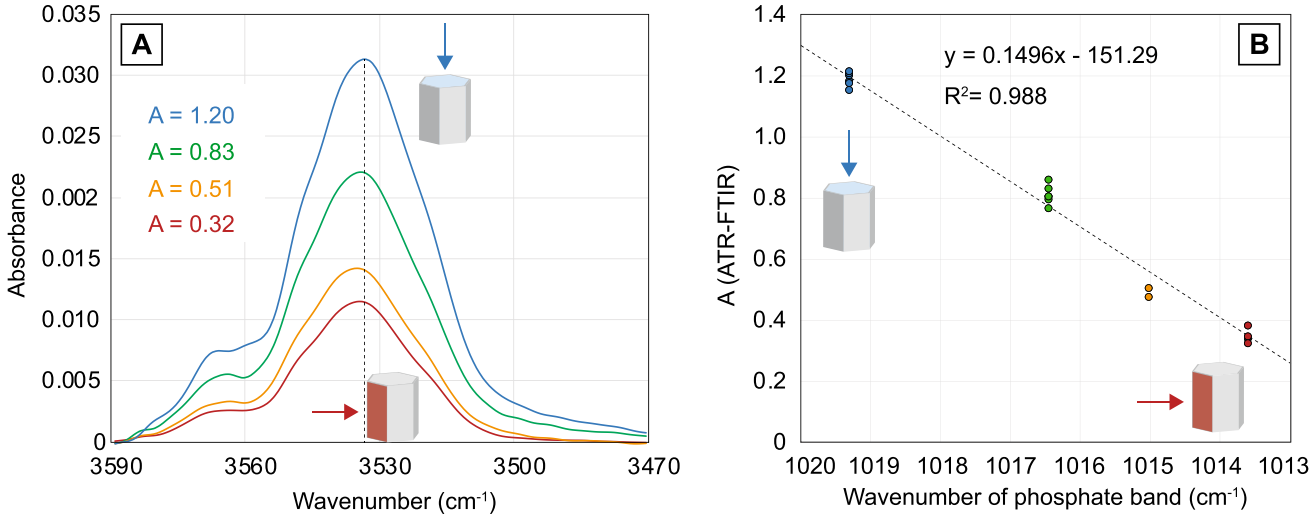

Fig. 5 **A** IR absorbance of "H_2O" bands of VOH apatite measured along different crystallographic orientations (blue IR spectrum = measured parallel to c-axis and red IR spectrum = measured perpendicular to c-axis). The integrated area of the absorption bands varies from 1.20 when measured parallel to the c-axis to 0.32 when measured perpendicular to the c-axis. **B** H_2O spectra area vs. wavenumber of the phosphate absorption band. Analyses perpendicular to c-axis produce a phosphate band at ~ 1013.7 cm^{-1}, while analyses parallel to c-axis leads to a band shift to ~ 1019.4 cm^{-1} (see also Fig. 2). The absorption area and crystallographic orientation are linearly correlated

perpendicular to the c-axis), both forced through the zero intercept of the vertical and horizontal axes (Fig. 8). The horizontal axis shows the integrated absorption bands of CO_2 in the wavenumber region ~ 1560 to 1360 cm^{-1} obtained by ATR-FTIR (see above), and plotted along the vertical axis is the absolute CO_2 (wt%) content determined by NRA measurements (see Table 1). The linear calibration line for analyses perpendicular to the c-axis is constructed via NRA and ATR-FTIR analyses of apatite specimens GL, YAM, HAM, MT, and SAP3 (Fig. 8). The data are fit by the following equation:

$$CO_2(\text{wt\%}) = 0.32 \times A_{CO2}, \quad (1)$$

where A_{CO2} is the integrated area of the CO_2 bands between wavenumbers ~ 1560 to 1360 cm^{-1} (Fig. 3). The calibration line for ATR-FTIR analyses parallel to the c-axis is defined by apatite specimen YAM and SAP3 (Fig. 8) (note that ATR-FTIR analyses of HAM apatite were not used for the calibration as analyses of the prepared sample returned slightly heterogeneous A_{CO2} values), both of which exhibit two main CO_2 bands, whose heights are related to the crystallographic orientation (Fig. 3). For such apatite specimens, when measured parallel to their c-axis, the following equation can be employed to calculate their CO_2 contents:

$$CO_2(\text{wt\%}) = 0.40 \times A_{CO2}, \quad (2)$$

where A_{CO2} is the integrated CO_2 absorption band area. Our data suggest that the CO_2 band heights and the corresponding integrated absorption areas only change when apatite is analyzed parallel to its c-axis, with wavenumbers ≤ 1019 cm^{-1} for their phosphate band (see above and Fig. 4).

H_2O calibration

To calibrate the ATR-FTIR technique for the measurement of H_2O contents in apatite, we used H_2O measurements by ERD of several apatite specimens (HRZ, VOH, and MT), which we then compared with ATR-FTIR analyses. Similar to the

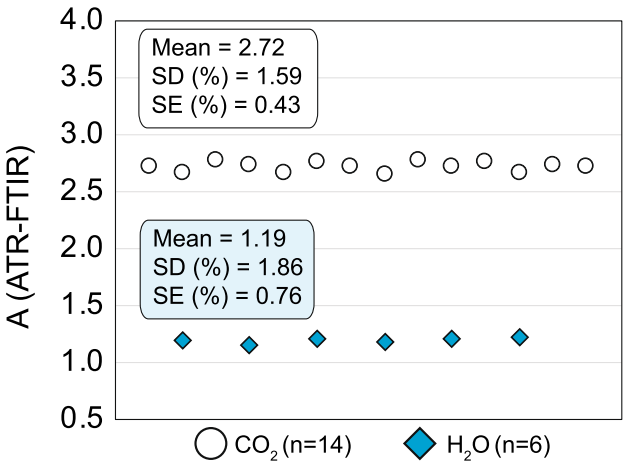

Fig. 6 Repeatability of CO_2 and H_2O ATR-FTIR analyses shown via the integrated area (A) of the IR absorption bands. White circular symbols represent CO_2 analyses and blue diamond symbols represent H_2O analyses

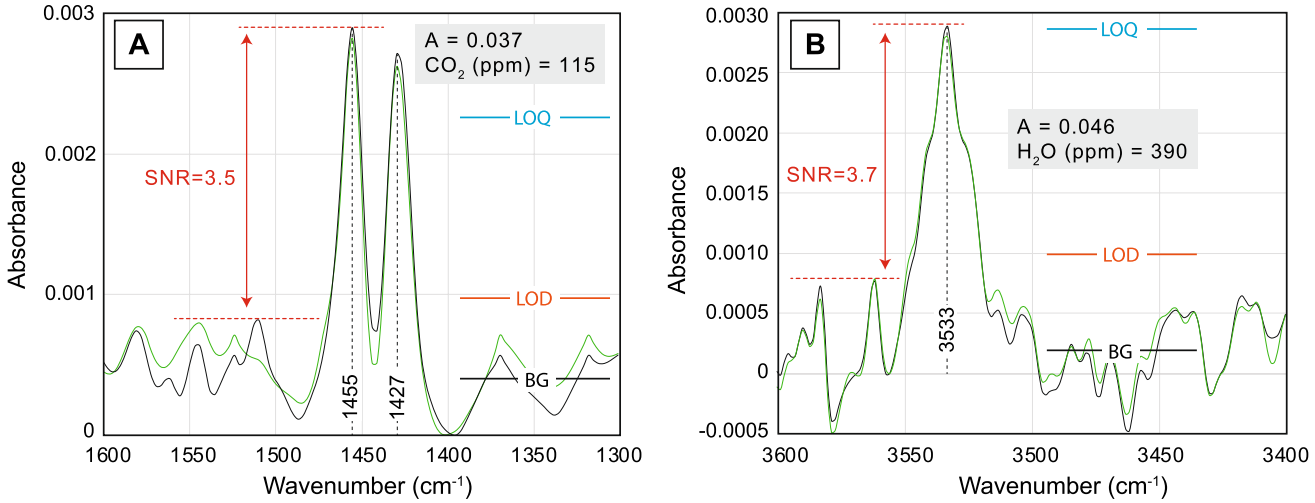

Fig. 7 **A** CO_2 IR absorption bands in an apatite grain of sample 19JH-03 (see main text for details on sample) analyzed perpendicular to its c-axis. The signal to noise ratio (SNR) of the background corrected wavenumber region is ~ 3.5 and the repeated analysis (green spectrum) produces indistinguishable absorption bands and SNR. Limit of quantification (LOQ) is defined as the average of the background signal (BG) plus ten times the standard deviation of the background signal in the wavenumber region 1600–1300 cm^{-1}. The limit of detection (LOD) is calculated as the average BG signal plus three times its standard deviation. **B** H_2O IR absorption band of HOI apatite (analyzed parallel to c-axis). SNR of the background corrected wavenumber region is ~ 3.7 and the repeated analyses (green spectrum) produces the same absorption and SNR. LOQ and LOD are calculated in the same way as for CO_2 in **A**

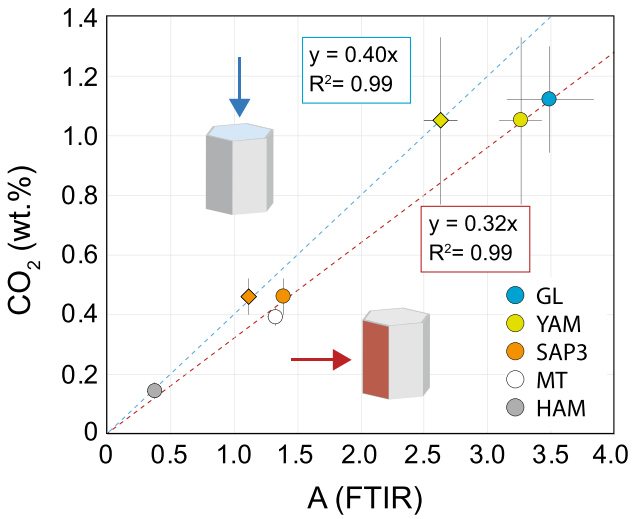

Fig. 8 Calibration lines for ATR-FTIR measurements of CO_2 in apatite. The vertical axis displays the CO_2 (wt%) content of apatite determined by NRA and the horizontal axis shows the area of the integrated IR absorption bands of CO_2 in the wavenumber region 1600–1300 cm^{-1}, when measured parallel (diamond symbols and corresponding blue regression line forced through the origin) and perpendicular (round symbols and corresponding red regression line forced through the origin) to their c-axis. Uncertainties are shown at the 95% CI

CO_2 calibration (see section above), ATR-FTIR analyses were performed along transects across the different apatite specimens, orientated parallel and perpendicular to the c-axis to test their homogeneity. The integrated H_2O absorbance bands for analyses parallel to the c-axis are 0.22 ± 0.01 (2SD) (n = 12) for HRZ, 1.19 ± 0.06 (n = 11) for VOH, and 1.22 ± 0.06 (n = 13) for MT. The integrated H_2O absorbance bands measured perpendicular to the c-axis are 0.34 ± 0.02 (2SD) (n = 13) and 0.33 ± 0.02 (2SD) (n = 10) for MT and VOH, respectively. Our data show that absolute H_2O values in apatite are linearly correlated with the integrated absorption area of the H_2O bands (Fig. 9) (FTIR spectra can be found in supplementary Fig. A-1). Similar to the approach by Wang et al. (2011), we integrated all absorbance bands between wavenumbers 3400 and 3600 cm^{-1}, accounting for all OH bonds, such as OH–F, OH–Cl, and others (see e.g., Tacker 2004; Fleet 2017). The calibration was forced through the zero intercept of the horizontal and vertical axis. Absolute H_2O concentration in apatite for analyses parallel to the c-axis can be calculated via the following equation:

$$H_2O(wt\%) = 0.85 \times A_{H2O}, \quad (3)$$

where A_{H2O} is the integrated absorption area of H_2O in the wavenumber region between 3470 and 3590 cm^{-1} (Fig. 9). The absorption bands of H_2O in apatite, when measured perpendicular to the c-axis, are less pronounced compared to measurements parallel to the c-axis (see above and Fig. 5). Accordingly, the slope of the calibration line for calculating absolute H_2O contents in apatite becomes significantly steeper (Fig. 9) resulting in the equation:

$$H_2O(wt\%) = 3.06 \times A_{H2O}, \quad (4)$$

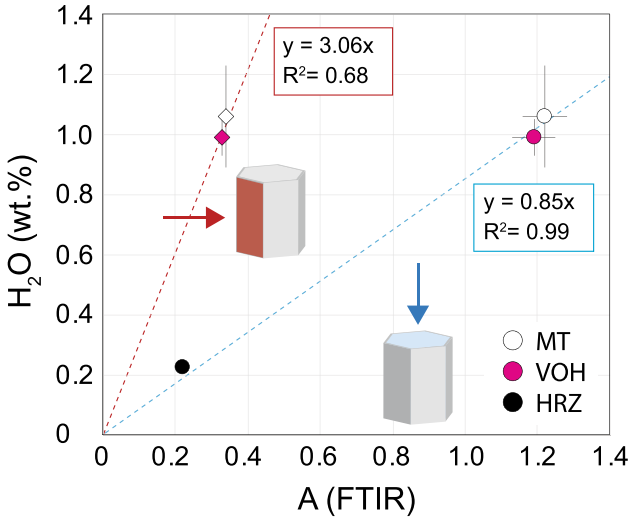

Fig. 9 Calibration line for ATR-FTIR measurements of H_2O in apatite. The vertical axis displays the absolute H_2O (wt%) content of apatite determined by ERD and the horizontal axis shows the area of the IR absorption bands of H_2O when analyzed parallel (round symbols and corresponding blue regression line forced through the origin) and perpendicular (diamond symbols and corresponding red regression line forced through the origin) to the c-axis. Uncertainties are shown at the 95% CI

where A_{H2O} is the integrated IR absorption area of H_2O in apatite. Note that this calibration line (Eq. 4) is anchored by two apatite specimens (MT and VOH) and the zero intercept of the vertical and horizontal axes, since the H_2O content of HRZ is too low to produce H_2O absorption bands when measured perpendicular to the c-axis (see discussion). In contrast to the absorption of the CO_2 bands, the H_2O absorption is consistently (and to a greater degree) affected when measured along different crystallographic orientations (see also sections above and Fig. 5).

The corrected H_2O absorption ($A_{H2Ocorr}$), for randomly orientated apatite grains can be calculated based on the phosphate absorption band position. Figure 5B shows that there is a linear relationship of absorption with wavenumber of the phosphate peak. The best approach for measuring a sample where the crystallographic orientation of apatite is not clear is to measure multiple grains in random orientation, fit a linear line through the data points and obtain an absorption value at the high wavenumber of 1019 cm^{-1} to 1022 cm^{-1}, representing the phosphate absorption band parallel the c-axis. For rare cases, where only a single measurement is possible, a corrected absorption parallel the c-axis can be retrieved from a random orientation via the following equation:

$$A_{H2Ocorr} = A_{H2Omeas} \times 8/\left(\nu_{phos} - 1011.13\right), \quad (5)$$

where $A_{H2Omeas}$ is the measured integrated peak area of H_2O of the unknown in the random orientation and ν_{Phos} is the wavenumber of the phosphate band in the random orientation. The value of 1011.3 derives from the *x*-axis intercept of the best fit regression of the random grains shown in Fig. 5B, while the scaling factor 8 is the difference between the 1019 cm^{-1} of the phosphate absorption band position parallel the c-axis and the intercept at 1011 cm^{-1}. $A_{H2Ocorr}$ can then be taken to calculate the absolute H_2O content via Eq. 3 used for H_2O quantification parallel to the c-axis. However, it has to be considered that the wavenumbers of the PO_4 band can be slightly dissimilar in different samples. For example, measurements perpendicular to c-axis can result in a phosphate band at ~ 1013 cm^{-1} to ~ 1016 cm^{-1}, and 1019 cm^{-1} to 1022 cm^{-1} for analysis parallel to their c-axis. Given this uncertainty we, therefore, recommend, if possible, analyzing apatite either parallel or perpendicular to their crystallographic orientations and using equation five only in cases where no other measurements are possible.

Discussion

CO_2 and H_2O IR absorption bands

Absorption bands of CO_2

Previous studies assigned IR absorption bands in the wavenumber region ~ 1560 cm^{-1} to ~ 1360 cm^{-1} to different CO_3^{2-} substitutions in apatite. CO_3^{2-} type A substitutions are located in the c-axis structural channel (the anion site), while type B CO_3^{2-} substitutes for PO_4 (e.g., Fleet and Liu 2003; Fleet et al. 2004; Tacker 2008 for a summary). Type-A CO_3^{2-}substitutions can be subdivided into type A1 and type A2, which produce IR absorption bands at ~ 1540 cm^{-1} and ~ 1450 cm^{-1} (type A1) and ~ 1563 cm^{-1} and 1506 cm^{-1} (Type A2) (Fleet et al. 2004). Both types sit in the channel position, however, type A2 is suggested to charge compensate the substitution of CO_3^{2-} for PO_4 and sits in a stuffed channel position (Fleet et al. 2004). A main IR absorption band for type B (termed type B2 in Tacker 2008) PO_4 is present at wavenumbers ~ 1455 cm^{-1} to 1450 cm^{-1} (Fleet et al. 2004) and a second type B band exists between wavenumbers 1430 cm^{-1} and 1405 cm^{-1}, however, its exact position is likely controlled by the composition of apatite (Tacker 2008 and references therein). The latter band, in the wavenumber region between 1430 and 1405 cm^{-1}, can be further subdivided into type B1 and type B2 substitutions with wavenumbers of ~ 1427 and ~ 1408 cm^{-1}, respectively, as elucidated in the example by Tacker (2008). These two subtypes of type B substitutions likely represent different crystallographic positions of carbonate at the PO_4 site (Fleet et al. 2004; Tacker 2008; Fleet and Liu 2003).

While it is outside the scope of this study to assign all of the individual absorption bands to different CO_2 bonds

and vibration modes, we suggest that some of the bands can be assigned to specific (sub-) type carbonate substitutions. Peak deconvolution (e.g., Tollan and Hermann 2019) of the ATR-FTIR spectra show that the IR absorption of CO_2 in the wavenumber region 1560 to 1360 cm^{-1} is the result of an estimated ten different absorption peaks (Fig. 10A'–C'). For example, Band 1, with a peak position at 1497 cm^{-1}, likely represents type A2 substitution and Bands 7 (1432 cm^{-1}) and 8 (1429 cm^{-1}) are type B2 carbonate substitutions, while Band 10 (1406 cm^{-1}) represents a type B1 carbonate substitution. The complexity of the CO_2 IR spectrum of apatite shows that many different substitutions are possible, which likely produce several absorption bands, some of which may need further experiments in combination with spectroscopy analyses to be better understood. Below we give a first order interpretation of the measured spectra.

Apatite specimen SAP3 and YAM (Fig. 3) show distinct type B2 doublet CO_3^{2-} absorption bands (Fig. 10A, B). However, the apparent type B2 absorption band (using the nomenclature by Tacker 2008) at ~ 1456 cm^{-1} likely overlaps with the absorption of CO_3^{2-} type A1 substitution (c.f., Tacker 2008 and references therein and band 3 in Fig. 10A'). HOI apatite shows a shoulder on the B2 peak (1430.5 cm^{-1}), likely caused by a B1 absorption band (band 10 in Fig. 10b', c.f., Tacker 2008). The HOI spectra also show a broad peak at higher wavenumbers (~ 1500 cm^{-1}), which can be assigned to type A2 CO_3^{2-} substitution (band 1 in Fig. 10B'). CO_3^{2-} IR spectra of apatite specimens MT and GL (Figs. 3 and 10C) are more complex. The absorption band at ~ 1438 cm^{-1} is difficult to assign to a certain CO_3^{2-} type substitution, however, the absorption band at ~ 1419 cm^{-1} likely represents type B1 CO_3^{2-} substitution. CO_3^{2-} type A1 substitution absorption bands form a distinct peak at ~ 1470 cm^{-1} (band 3 in Fig. 10C'), with absorption peaks on its shoulders, potentially representing type B2 and type A2 CO_3^{2-} substitutions (Fig. 10C). In all specimens, IR absorption of type B2 (and type A) CO_3^{2-}substitutions increase when apatite is analyzed perpendicular to the c-axis. The only IR absorption band that increases when apatite is analyzed parallel to the c-axis is located at a wavenumber of ~ 1438 cm^{-1} in the MT and GL apatite (Fig. 10C).

Absorption bands of H_2O

The IR absorption bands of H_2O in apatite are less complex than those for CO_2. Nevertheless, multiple absorption bands related to OH vibration are routinely observed, with the absorption of OH-F vibration bands (~ 3533 cm^{-1}) typically resulting in the most significant peak (Fig. 1 and see Tacker 2004). The deconvoluted spectra suggest that the main "OH-F" band in the IR spectra is composed of at least three absorption peaks (bands 3–5, see legend of Figs. 11A', B'), and we speculate that all of them are related to OH-F bonds in apatite, since all samples contain these three bands that make up the main peak. Based on previous studies (e.g., Tacker 2004 and references therein), peak 2 can be assigned to OH-OH vibration at ~ 3566 cm^{-1}, as for example observed in VOH apatite (Fig. 11A). Peak 6 is attributed to OH-Cl bonds, (Fig. 11A', B'). The absence of peak 6 in VOH apatite agrees with EPMA results suggesting a low Cl content, whereas HRZ apatite contains ~ 0.6 wt% Cl (Table 2), which likely leads to the absorption peak 6. According to Tacker (2004) the absorption peak 7 at a wavelength of ~ 3470 cm^{-1} most likely reflects OH-REE bonds (Fig. 11B). Indeed, HRZ apatite contains several wt% REEs (Hammerli, unpublished data).

Quantification of CO_2 and H_2O by ATR-FTIR

For the quantification of CO_2 and H_2O in apatite we followed a similar approach as described in the transmission FTIR studies by Clark et al. (2016) and Wang et al. (2011), in which the absorption areas of the H_2O and CO_2 peaks in the wavenumber regions of ~ 3600 cm^{-1} to 3500 cm^{-1} and 1500 cm^{-1} to 1350 cm^{-1} are calibrated against ERD and NRA CO_2 and H_2O measurements, respectively. The ATR-FTIR method for measuring CO_2 and H_2O, described in this study, bears two main advantages over transmission FTIR techniques. First, samples are not required to be prepared as wafers polished on both sides. FTIR analyses in ATR mode can be directly conducted on polished surfaces, for example on apatite in polished thin sections or in epoxy mounts. Second, the PO_4 peak does not lead to total absorbance in apatite spectra generated by ATR-FTIR measurements (Fig. 1) and can, therefore, be used to determine the crystallographic orientation of the analyzed sample. This means that the CO_2 and H_2O absorption bands of randomly orientated apatite can be corrected for crystallographic effects (see sections above).

Conversely, the main advantage of transmission FTIR is that lower concentrations can be measured, which can be in the ppm and sub-ppm range for H_2O and CO_2, respectively (Wang et al. 2011; Clark et al. 2016), while the limit of quantification for ATR-FTIR analysis is estimated to be ~ 400 ppm for H_2O, when measured parallel to the c-axis and ~ 100 ppm for CO_2, when measured perpendicular to the c-axis (see above). However, minimum detection and quantification limits, especially for H_2O, are likely to some degree governed by the H_2O absorbance band shape. The signal to background ratio from narrow H_2O absorbance bands is higher than for wider or separated absorbance bands, even if the H_2O content in all three scenarios are the same, hence a lower limit of quantification can be achieved in the former case. If no absorption is detected with the ATR-FTIR analysis, this gives valuable information for the sample preparation for transmission measurements in terms of sample thickness of the doubly polished wavers.

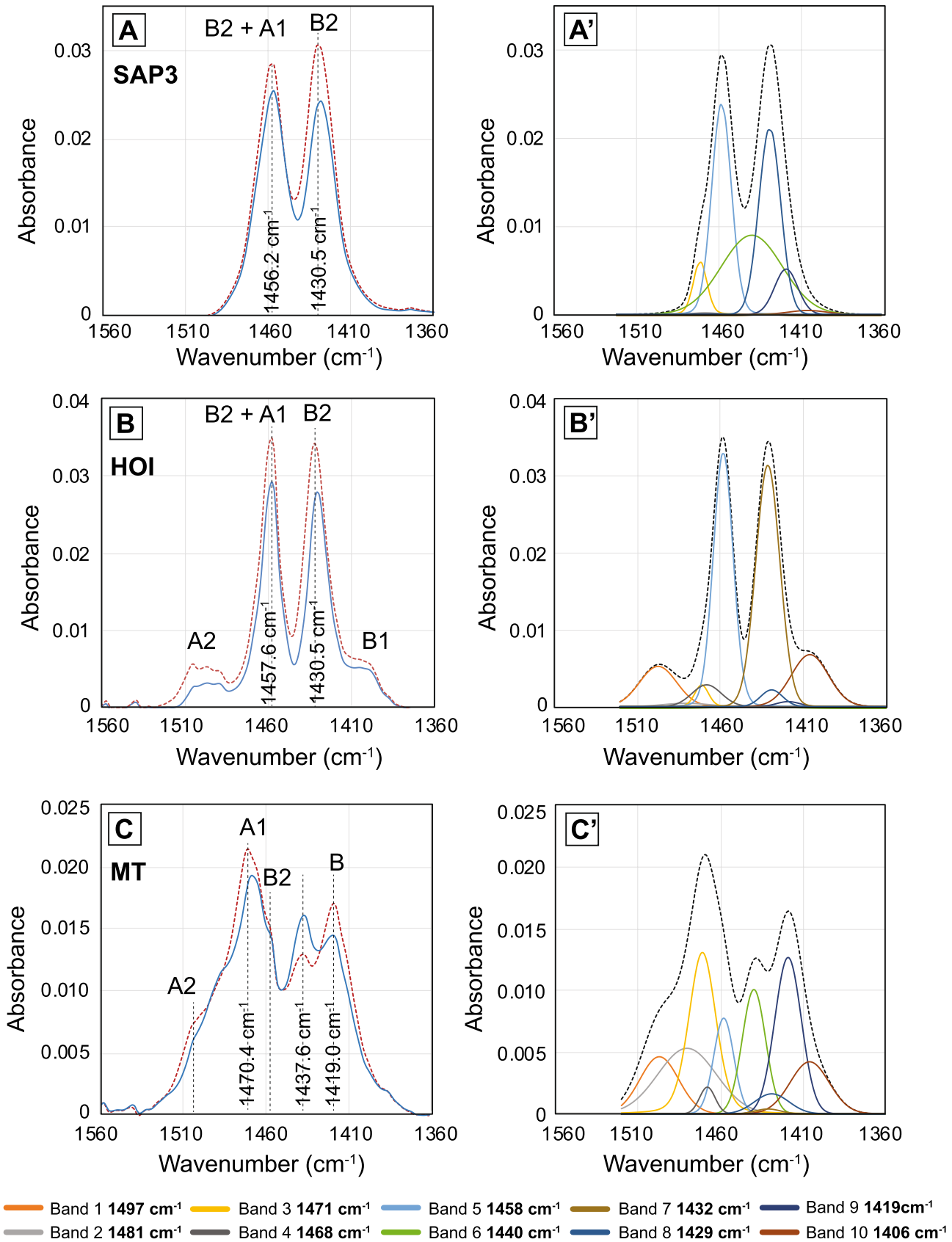
A
SAP3
B2 + A1
B2
1456.2 cm-1
1430.5 cm-1
A'
B
HOI
A2
1457.6 cm-1
B1
B'
C
MT
A1
B2
B
1470.4 cm-1
1437.6 cm-1
1419.0 cm-1
C'
Absorbance
Wavenumber (cm-1)
Band 1 1497 cm-1
Band 2 1481 cm-1
Band 3 1471 cm-1
Band 4 1468 cm-1
Band 5 1458 cm-1
Band 6 1440 cm-1
Band 7 1432 cm-1
Band 8 1429 cm-1
Band 9 1419cm-1
Band 10 1406 cm-1

◂ **Fig. 10** IR CO_2 absorption bands when measured along the c-axis (blue line) and perpendicular to the c-axis (dotted red line) in SAP3 (**A**), HOI (**B**), and MT (**C**) apatite, with assigned CO_2 substitutions A1, A2, B1, and B2 (see text). **A'–C'** show the same spectra "deconvoluted", defined by ten individual absorption peaks (see text). The black dotted line in **A'–C'** shows the sum of all modeled spectra

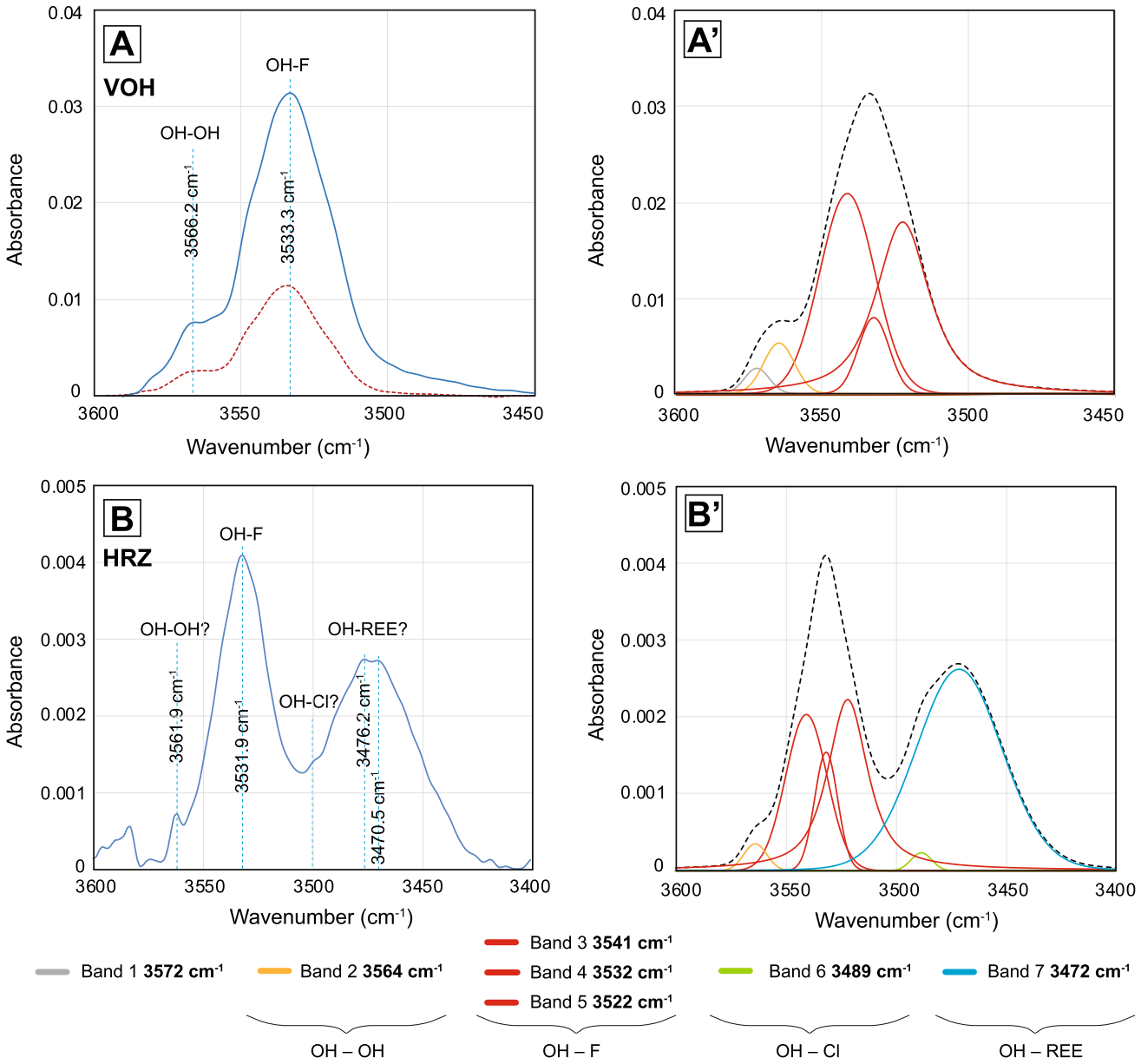

Fig. 11 IR H_2O absorption bands when measured along the c-axis (blue line) and perpendicular the c-axis (dotted red line) in **A** VOH (~0.98 wt% H_2O) and **B** HRZ apatite (~0.22 wt% H_2O) with inferred OH vibration bands based on literature data (see main text). **A'** and **B'** are the same spectra "deconvoluted", defined by seven individual absorption bands (see text). The black dotted line in **A'–C'** shows the sum of all modeled spectra

Comparison of H_2O determination by EPMA vs. ATR-FTIR

As discussed before, measuring and calculating H_2O concentrations of apatite is challenging, with the most routine approach for constraining H_2O being the stoichiometric method based on EPMA measurements (see above and Ketcham 2015). Conducting ATR-FTIR H_2O analysis at the same location as EPMA measurements allows for an assessment of the accuracy of EPMA-derived H_2O concentrations (see Table 2). Figure 12 shows H_2O (wt%) determined by ERD and FTIR vs. H_2O calculated via stoichiometric constraints based on EPMA measurements. Note that all apatite grains were measured perpendicular to their c-axis as

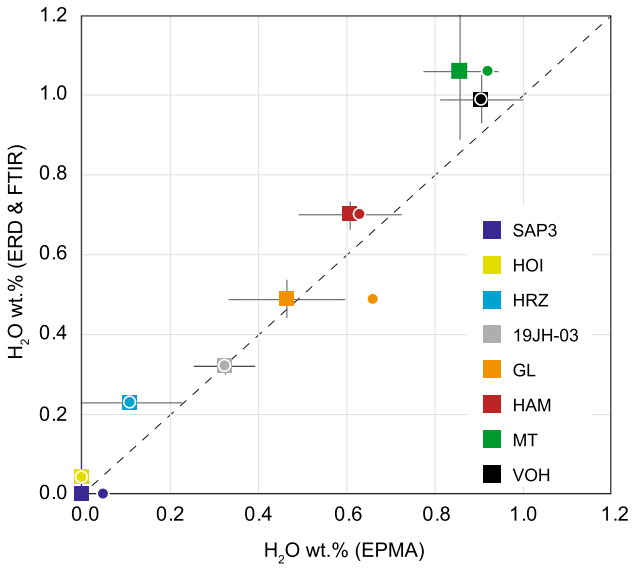

Fig. 12 H_2O determined by ERD and FTIR vs. H_2O constrained by the stoichiometry of apatite based on EPMA measurements perpendicular to the c-axis. Square symbols represent stoichiometric H_2O calculation when CO_2 contents of apatite are considered (see Table 2) and round symbols show H_2O determination when CO_2 contents are ignored. Uncertainties are 2SD of multiple ERD (Table 1) measurements or FTIR analyses perpendicular to the c-axis across a grain of the respective sample (2SD are the same for both symbol types). Note that for apatite SAP3, the uncertainty for stoichiometric H_2O quantification based on EPMA measurements by ignoring its CO_2 content is ± 0.12 wt%. H_2O. HOI values determined by FTIR are based on the spectra shown in Fig. 7 and 19JH-03 values are taken from Fig. 13

suggested by Goldoff et al. (2012). Our data (Fig. 12) show that the calculation of H_2O in apatite when following the methods by Goldoff et al. (2012) and Ketcham (2015), and by accounting for CO_2 on the anion site, leads to an overall good agreement between absolute methods (NRA and FTIR) and the EPMA approach (i.e., data of the different approaches are within ~ 20%, Fig. 11) for all studies apatite specimens with variable compositions. When the CO_2 content of apatite is not known, the stoichiometric calculation of H_2O can in some cases lead to an overestimation of the H_2O content. The reason is that the CO_2 at the anion site is not accounted for and hence the calculated H_2O content at this site is too high (see Fig. 12).

Examples

CO_2 and H_2O content in apatite of carbonatitic rocks

CO_2 and H_2O play a major role in carbonatitic systems (Jones et al. 2013 for a review). For example, experiments have revealed that the solidus of carbonatitic melt is lowered by water (Poli 2015) and Martin et al. (2013) have shown that H_2O is key for the immiscibility of parental magma of carbonatitic melt and also for enriching carbonatitic melt in REE. However, recognizing conjugate silicate and carbonatite melt, due to immiscibility is often challenging in natural settings due to post emplacement modifications of the intrusions (e.g., Martin et al. 2012). Besides melt inclusions, apatite, typically a major REE phase in carbonatitic rocks and igneous rocks in general, is a promising mineral to record CO_2 and H_2O contents of carbonatitic melt (see, e.g., Chakhmouradian et al. 2017; Santos and Clayton 1995; Broom-Fendley et al. 2020). Measuring the volatile content of apatite via combined EPMA (Cl, F) and ATR-FTIR (CO_2, H_2O) analyses might be a helpful tool for further understanding the formation of carbonatites, and especially the immiscibility of carbonatite and silicate melt, as well as post emplacement alteration and element redistribution (Broom-Fendley et al. 2016, 2020). For example, the composition of apatite of the Mud Tank (MT) carbonatite in the Strangway Ranges, Northern Territory, Australia, suggests that MT apatite formed from a hydrous melt, as MT apatite contains ~ 1 wt% H_2O and ~ 0.4 wt% CO_2 (Tables 1 and 2). While the CO_2 content of MT apatite is very similar to other published CO_2 concentrations of carbonatitic apatite (Binder and Troll; 1989; Santos and Clayton 1995), the H_2O content of MT apatite is significantly higher (by a factor 4) than in "typical" carbonatite apatite (Binder and Troll 1989). By assuming that the MT apatite retained its original geochemical fingerprint, a hypothesis supported by the mantle-like oxygen isotope signatures and the absence of alteration zones (Yang et al. 2020), we speculate that the Mud Tank carbonatite did not exsolve significant amounts of hydrous fluids, at least at the currently-exposed stratigraphic level. This would also explain the lack of significant alteration of the gneissic host rocks in agreement with earlier interpretations by Crohn and Moore (1984). Future studies of CO_2 and H_2O contents in apatite at different stratigraphic levels of (carbonatitic) intrusions, might be useful to trace degassing and fluid exsolution processes during the emplacement of igneous rocks to trace, for example, proximal hydrothermal alteration and ore genesis by hydrothermal fluids. In addition, and given the seemingly universal elevated CO_2 in apatite of alkaline and carbonatitic rocks (e.g., Binder and Troll 1989; Santos and Clayton 1995; Broom-Fendley et al. 2020, this study), quantifying CO_2 via FTIR might be a useful tool for REE deposit exploration following a similar approach as described in Mao et al. (2016).

CO_2 and H_2O in apatite of metamorphic rocks

Fluids and their compositions play a central role during prograde metamorphism. Metamorphic degassing in collisional orogens likely contributes significantly to the atmosphere's CO_2 budget (e.g., Kerrick and Caldeira 1998; Perrier et al. 2009; Skleton 2011; Groppo et al. 2017; Stewart and Ague

2018). Modeling fluid compositions is challenging in heterogeneous rock types, such as in metasedimentary lithologies, as compositional changes on the thin section-scale lead to a range of attempted local equilibrium reactions between fluids and minerals. An alternative and complementary approach to geochemical modeling of fluid compositions is probing minerals, such as apatite, which can act as an archive of fluid compositions. To test the feasibility of our method in metamorphic rocks we analyzed a metasedimentary sample of the Bündnerschiefer Formation (BdsF) of the Central Alps. Rocks of the BdsF are typically formed during prograde Alpine metamorphism of marine sediments. Our sample (19JH-03) comes from metamorphosed Bündnerschiefer at Campolungo that underwent peak pressure and temperature conditions of 620 °C and 6.5 kbar at peak temperature (Todd and Engi 1997). It contains large (~ 1 cm) garnet porphyroblasts within fine-grained layers composed of quartz, plagioclase, zoisite, rutile, biotite, and minor sulfides alternating with predominantly calcite bearing layers. Sample 19JH-03 shows no indications of significant alteration or regression and hence the mineral assemblage likely represents peak metamorphic conditions. We analyzed the cores of apatite from mineral separates parallel and perpendicular to their c-axis by ATR-FTIR to test if apatite minerals record CO_2 and H_2O during metamorphism (Fig. 13).

The results show that the H_2O content in apatite is relatively uniform at ~ 0.30–0.33 wt%, which suggests that apatite attempted to reach equilibrium in the presence of a fluid at ~ 620 °C, which agrees with the findings of Hammerli et al. (2014). CO_2 contents in 19JH-03 apatite vary between ~ 100 and ~ 600 ppm (Fig. 13C) and in light of the uniform H_2O content, variability of CO_2 concentrations likely suggests variable aCO_2 in metamorphic fluids on a cm-scale. While we are unable to quantify aCO_2 in the metamorphic fluid during metamorphism based on apatite compositions, mainly due to the lack of established CO_2 partition coefficients, this example illustrates that H_2O and CO_2 contents in metamorphic rocks can be systematically and qualitatively studied via ATR-FTIR, which is useful to probe the enigmatic CO_2 release during metamorphism (e.g., Ramos et al. 2020; Stewart and Ague 2020) via the presence of CO_2 in metamorphic apatite.

Summary and future implications

We calibrated the CO_2 and H_2O ATR-FTIR spectra of polished apatite specimens to absolute CO_2 and H_2O concentrations. The apatite compositions used for the calibration of the ATR spectra varied from F-rich specimens (YAM, SAP3) to hydroxy-rich samples (MT, VOH), covering most common apatite compositions in igneous and metamorphic rocks (e.g., Piccoli and Candela 2002; Spear and Pyle 2002). However, it would be useful to develop further standards for H_2O and CO_2 measurements by ATR-FTIR of Cl-rich apatite, with significantly higher Cl contents than those analyzed in the current study (~ 0.6 wt%, Table 2).

Importantly, all ATR-FTIR spectra in this study were produced using a Ge crystal in the ATR module with an internal reflection angle of 21.5°–37° (see methods). Therefore, using different ATR modules and crystal-types with different internal reflection angles will likely require recalibration of the absorbance areas of the spectra to absolute CO_2 and H_2O values. Our data show a linear relationship between the integrated area of the CO_2 and H_2O absorption bands and the absolute CO_2 and H_2O concentrations determined by NRA and ERD, respectively, which can be used to directly calculate CO_2 and H_2O contents in apatite from their FTIR spectra. The crystallographic orientation of apatite can be determined via the

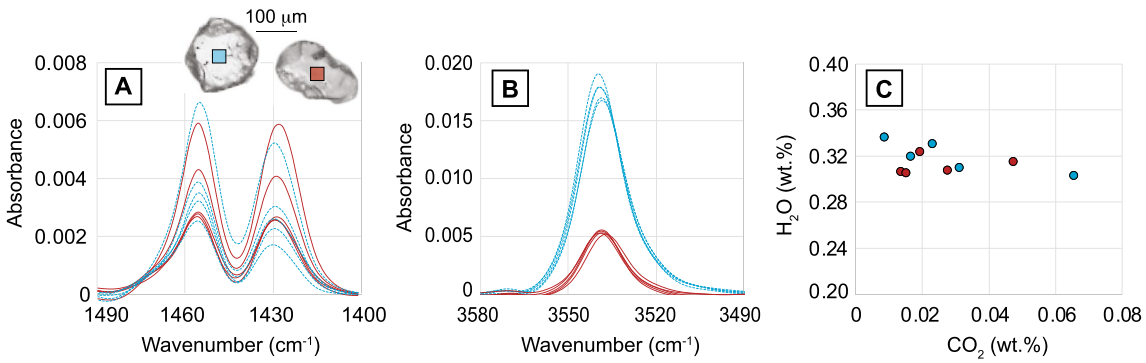

Fig. 13 **A** IR CO_2 absorption bands of apatite in sample 19JH-03 (including typical apatite morphologies and analytical sites of their cores) and **B** IR H_2O absorption bands of the same apatite grains as shown in **A**. Dotted blue lines in **A** and **B** represent analyses parallel to the c-axis of apatite grains ($n = 5$) and red lines show analyses perpendicular to the c-axis of different apatite grains ($n = 5$). **C** H_2O and CO_2 concentrations of the analyzed apatite grains of sample 19JH-03. Blue circles represent analyses parallel to the c-axis and red circles are H_2O and CO_2 concentrations of apatite grains measured perpendicular to the c-axis

band position of the phosphate IR absorption band, which can be used to account for crystallographic effects on the acquired CO_2 and H_2O IR absorption bands, permitting the accurate measurement of CO_2 and H_2O contents of randomly orientated apatite grains. With the analytical conditions used in this study, the limit of quantification for CO_2 is ~ 100 ppm and ~ 400 ppm for H_2O. This new ATR-FTIR approach will allow for routine in situ CO_2 and H_2O characterization of apatite with a spatial resolution of ~ 35 µm on polished sample surfaces, which permits the systematic study of CO_2 and H_2O of apatite in a wide range of geological environments. Together with other micro-analytical methods, FTIR in ATR mode is a useful tool to further develop apatite CO_2 and H_2O contents as a proxy for aCO_2 and aH_2O in fluids via partition coefficients. To further understand which factors control different substitutions and CO_2 partitioning, the quantification of A- and B-type CO_2 substitutions may be possible via systematic studies and specific calibration of the respective absorption bands in the future. A further development of the technique would be combining the ATR-FTIR method described here with a focal plane array (FPA) mapping detector, rather than the MCT detector used here. While the FPA detector has lower sensitivity, potentially increasing the LOQ, it offers significantly higher spatial resolution (down to ~ 1 × 1 µm). This would open up further possibilities of analyzing extremely small apatite grains, such as those included in other minerals, and thus more likely to preserve primary CO_2 contents, even in samples that underwent several thermal events. Combining the CO_2 and H_2O contents of apatite with other volatiles and halogens (S, Cl, F, Br, I) (e.g., Zhu and Sverjensky 1991; McCubbin et al. 2015; Kusebauch et al. 2015; Li and Hermann 2015, 2017; Riker et al. 2018; Li and Costa 2020; Hammerli et al. 2021) makes apatite a particularly promising and useful mineral to study fluid properties and fluid transfer in a large range of geological environments.

Supplementary Information The online version contains supplementary material available at https://doi.org/10.1007/s00410-021-01858-6.

Acknowledgements We thank anonymous reviewers for their constructive comments and the editor Timm John for handling this paper. This work was supported by Swiss National Science Foundation grant PZ00P2_180095 to J.H. Prof. B. Hofmann from the NMB and K. Thrane from the Geological Survey of Denmark and Greenland are thanked for providing apatite material for this study. P. Lanari is thanked for help with EPMA measurements.

Funding Open access funding provided by University of Bern.

Open Access This article is licensed under a Creative Commons Attribution 4.0 International License, which permits use, sharing, adaptation, distribution and reproduction in any medium or format, as long as you give appropriate credit to the original author(s) and the source, provide a link to the Creative Commons licence, and indicate if changes were made. The images or other third party material in this article are included in the article's Creative Commons licence, unless indicated otherwise in a credit line to the material. If material is not included in the article's Creative Commons licence and your intended use is not permitted by statutory regulation or exceeds the permitted use, you will need to obtain permission directly from the copyright holder. To view a copy of this licence, visit http://creativecommons.org/licenses/by/4.0/.

References

Aubaud C, Bureau H, Raepsaet C, Khodja H, Withers AC, Hirschmann MM, Bell DR (2009) Calibration of the infrared molar absorption coefficients for H in olivine, clinopyroxene and rhyolitic glass by elastic recoil detection analysis. Chem Geol 262:78–86

Barnes JJ, Tartèse R, Anand M et al (2014) The origin of water in the primitive Moon as revealed by the lunar highlands samples. Earth Planet Sci Lett 390:244–252. https://doi.org/10.1016/j.epsl.2014.01.015

Berkesi M, Guzmics T, Szabó C et al (2012) The role of CO2-rich fluids in trace element transport and metasomatism in the lithospheric mantle beneath the Central Pannonian Basin, Hungary, based on fluid inclusions in mantle xenoliths. Earth Planet Sci Lett 331–332:8–20. https://doi.org/10.1016/j.epsl.2012.03.012

Binder G, Troll G (1989) Coupled anion substitution in natural carbon-bearing apatites. Contrib Miner Petrol 101:394–401. https://doi.org/10.1007/BF00372213

Boyce JW, Liu Y, Rossman GR et al (2010) Lunar apatite with terrestrial volatile abundances. Nature 466:466–469. https://doi.org/10.1038/nature09274

Broom-Fendley S, Styles MT, Appleton JD et al (2016) Evidence for dissolution-reprecipitation of apatite and preferential LREE mobility in carbonatite-derived late-stage hydrothermal processes. Am Miner 101:596–611. https://doi.org/10.2138/am-2016-5502CCBY

Broom-Fendley S, Siegfried PR, Wall F et al (2020) The origin and composition of carbonatite-derived carbonate-bearing fluorapatite deposits. Min Depos 56:864–884. https://doi.org/10.1007/s00126-020-01010-7

Bureau H, Raepsaet C, Khodja H, Carraro A, Aubaud C (2009) Determination of hydrogen content in geological samples using elastic recoil detection analysis (ERDA). Geochim Cosmochim Acta 73:3311–3322

Capriolo M, Marzoli A, Aradi LE et al (2020) Deep CO2 in the end-Triassic Central Atlantic Magmatic Province. Nat Commun 11:1670. https://doi.org/10.1038/s41467-020-15325-6

Carvalho BB, Bartoli O, Cesare B et al (2020) Primary CO_2-bearing fluid inclusions in granulitic garnet usually do not survive. Earth Planet Sci Lett 536:116170. https://doi.org/10.1016/j.epsl.2020.116170

Chakhmouradian AR, Reguir EP, Zaitsev AN et al (2017) Apatite in carbonatitic rocks: compositional variation, zoning, element partitioning and petrogenetic significance. Lithos 274–275:188–213. https://doi.org/10.1016/j.lithos.2016.12.037

Cherniak DJ, Hervig RL, Koepke J, Zhang Y, Zhao D (2010) Analytical methods in diffusion studies. Rev Miner Geochem 72:107–170

Clark K, Zhang Y, Naab FU (2016) Quantification of CO2 concentration in apatite. Am Miner 101:2443–2451. https://doi.org/10.2138/am-2016-5661

Comodi P, Liu Y (2000) CO3 substitution in apatite: further insight from new crystal-chemical data of Kasekere (Uganda) apatite. Eur J Miner 12:965–974. https://doi.org/10.1127/0935-1221/2000/0012-0965

Crohn PW, Moore DH (1984) The Mud Tank carbonatite, strangways range, central Australia. BMR J Aust Geol Geophys 9:13–18
Csedreki L, Uzonyi I, Sziki GA, Szikszai Z, Gyurky G, Kiss AZ (2014) Measurements and assessment of 12C(d, pγ)13C reaction cross sections in the deuteron energy range 740–2000 keV for analytical applications. Nucl Instrum Methods Phys Res Sect B 328:59–64
Deer WA, Howie RA, Zussman J (2013) An introduction to the rock-forming minerals, 3rd edn. Berforts Information Press, Stevenage, Hertfordshire, UK, pp 498
Diamond LW (2001) Review of the systematics of CO2–H2O fluid inclusions. Lithos 55:69–99. https://doi.org/10.1016/S0024-4937(00)00039-6
Elliott JC (1994) Structure and chemistry of the apatites and other calcium orthophosphates. J Organomet Chem 188:C19–C20. https://doi.org/10.1016/S0022-328X(00)82820-X
Fleet ME (2017) Infrared spectra of carbonate apatites: Evidence for a connection between bone mineral and body fluids. Am Miner 102:149–157. https://doi.org/10.2138/am-2017-5704
Fleet ME, Liu X (2003) Carbonate apatite type A synthesized at high pressure: new space group (P3̄) and orientation of channel carbonate ion. J Solid State Chem 174:412–417. https://doi.org/10.1016/S0022-4596(03)00281-0
Fleet ME, Liu X, King PL (2004) Accommodation of the carbonate ion in apatite: an FTIR and X-ray structure study of crystals synthesized at 2–4 GPa. Am Miner 89:1422–1432. https://doi.org/10.2138/am-2004-1009
Fleet ME, Liu X, Liu X (2011) Orientation of channel carbonate ions in apatite: effect of pressure and composition. Am Miner 96:1148–1157. https://doi.org/10.2138/am.2011.3683
Fowler BO (1974) Infrared studies of apatites. I. Vibrational assignments for calcium, strontium, and barium hydroxyapatites utilizing isotopic substitution. Inorg Chem 13:194–207. https://doi.org/10.1021/ic50131a039
Freund F, Knobel RM (1977) Distribution of fluorine in hydroxyapatite studied by infrared spectroscopy. J Chem Soc Dalton Trans. https://doi.org/10.1039/dt9770001136
Goldoff B, Webster JD, Harlov DE (2012) Characterization of fluor-chlorapatites by electron probe microanalysis with a focus on time-dependent intensity variation of halogens. Am Miner 97:1103–1115. https://doi.org/10.2138/am.2012.3812
Groppo C, Rolfo F, Castelli D, Mosca P (2017) Metamorphic CO2 Production in Collisional Orogens: Petrological Constraints from Phase Diagram Modeling of Himalayan, Scapolite-bearing, Calc-silicate Rocks in the NKC(F)MAS(T)-HC system. J Petrol 58:53–83. https://doi.org/10.1093/petrology/egx005
Grunenwald A, Keyser C, Sautereau AM et al (2014) Revisiting carbonate quantification in apatite (bio)minerals: a validated FTIR methodology. J Archaeol Sci 49:134–141. https://doi.org/10.1016/j.jas.2014.05.004
Gulbrandsen RA, Kramer JR, Beatty LB, Mays RE (1966) Carbonate-bearing apatite from Faraday Township, Ontario, Canada. Am Miner 51:819–824
Gunasekaran S, Anbalagan G, Pandi S (2006) Raman and infrared spectra of carbonates of calcite structure. J Raman Spectrosc 37:892–899. https://doi.org/10.1002/jrs.1518
Hammerli J, Kemp AIS, Spandler C (2014) Neodymium isotope equilibration during crustal metamorphism revealed by in situ microanalysis of REE-rich accessory minerals. Earth Planet Sci Lett 392:133–142. https://doi.org/10.1016/j.epsl.2014.02.018
Hammerli J, Greber ND, Martin L et al (2021) Tracing sulfur sources in the crust via SIMS measurements of sulfur isotopes in apatite. Chem Geol. https://doi.org/10.1016/j.chemgeo.2021.120242
Hu S, Lin Y, Zhang J et al (2015) Measurements of water content and D/H ratio in apatite and silicate glasses using a NanoSIMS 50L. J Anal at Spectrom 30:967–978. https://doi.org/10.1039/C4JA00417E
Jones AP, Genge M, Carmody L (2013) Carbonate melts and carbonatites. Rev Mineral Geochem 75:289–322. https://doi.org/10.2138/rmg.2013.75.10
Kerrick DM, Caldeira K (1998) Metamorphic CO2 degassing from orogenic belts. Chem Geol 145:213–232. https://doi.org/10.1016/S0009-2541(97)00144-7
Ketcham RA (2015) Technical Note: Calculation of stoichiometry from EMP data for apatite and other phases with mixing on monovalent anion sites. Am Miner 100:1620–1623. https://doi.org/10.2138/am-2015-5171
Kusebauch C, John T, Whitehouse MJ et al (2015) Distribution of halogens between fluid and apatite during fluid-mediated replacement processes. Geochim Cosmochim Acta 170:225–246. https://doi.org/10.1016/j.gca.2015.08.023
Li W, Costa F (2020) A thermodynamic model for F-Cl-OH partitioning between silicate melts and apatite including non-ideal mixing with application to constraining melt volatile budgets. Geochim Cosmochim Acta 269:203–222. https://doi.org/10.1016/j.gca.2019.10.035
Li H, Hermann J (2015) Apatite as an indicator of fluid salinity: An experimental study of chlorine and fluorine partitioning in subducted sediments. Geochim Cosmochim Acta 166:267–297. https://doi.org/10.1016/j.gca.2015.06.029
Li H, Hermann J (2017) Chlorine and fluorine partitioning between apatite and sediment melt at 2.5 GPa, 800 °C: a new experimentally derived thermodynamic model. Am Miner 102:580–594. https://doi.org/10.2138/am-2017-5891
Li W, Costa F, Nagashima K (2000) Apatite crystals reveal melt volatile budgets and magma storage depths at Merapi volcano, Indonesia. J Petrol. https://doi.org/10.1093/petrology/egaa100
Mao M, Rukhlov AS, Rowins SM et al (2016) Apatite trace element compositions: a robust new tool for mineral exploration. Econ Geol 111:1187–1222. https://doi.org/10.2113/econgeo.111.5.1187
Martin LHJ, Schmidt MW, Mattsson HB et al (2012) Element partitioning between immiscible carbonatite–kamafugite melts with application to the Italian ultrapotassic suite. Chem Geol 320–321:96–112. https://doi.org/10.1016/j.chemgeo.2012.05.019
Martin LHJ, Schmidt MW, Mattsson HB, Guenther D (2013) Element partitioning between immiscible carbonatite and silicate melts for dry and H2O-bearing systems at 1–3 GPa. J Petrol 54:2301–2338. https://doi.org/10.1093/petrology/egt048
Mathez E, Blacic J, Beery J, Hollander M, Maggieore C (1987) Carbon in olivine. Results from nuclear reaction analysis. J Geophys Res 92(B5):3500–3506
Mayer M (1999) SIMNRA, a simulation program for the analysis of NRA, RBS and ERDA. In: Duggan JL, Morgan IL (eds) Application of accelerators in research and industry, Pts 1 and 2, vol 475. AIP Conference Proceedings American Institute of Physics, Melville, New York, pp 541–544
McCubbin FM, Vander Kaaden KE, Tartèse R et al (2015) Experimental investigation of F, Cl, and OH partitioning between apatite and Fe-rich basaltic melt at 1.0–1.2 GPa and 950–1000 °C. Am Miner 100:1790–1802. https://doi.org/10.2138/am-2015-5233
Pan Y, Fleet ME (2002) Compositions of the Apatite-Group minerals: substitution mechanisms and controlling factors. Rev Min Geochem 48:13–49. https://doi.org/10.2138/rmg.2002.48.2
Perrier F, Richon P, Byrdina S et al (2009) A direct evidence for high carbon dioxide and radon-222 discharge in Central Nepal. Earth Planet Sci Lett 278:198–207. https://doi.org/10.1016/j.epsl.2008.12.008
Phillips GN, Evans KA (2004) Role of CO2 in the formation of gold deposits. Nature 429:860–863. https://doi.org/10.1038/nature02644
Piccoli PM, Candela PA (2002) Apatite in igneous systems. Rev Min Geochem 48:255–292. https://doi.org/10.2138/rmg.2002.48.6

Poli S (2015) Carbon mobilized at shallow depths in subduction zones by carbonatitic liquids. Nat Geosci 8:633–636. https://doi.org/10.1038/ngeo2464

Popa R-G, Tollan P, Bachmann O, Schenker V, Ellis B, Allaz JM (2021) Water exsolution in the magma chamber favors effusive eruptions: application of Cl-F partitioning behavior at the Nisyros-Yali volcanic area. Chem Geol. https://doi.org/10.1016/j.chemgeo.2021.120170

Proust C, Husson E, Blondiaux G, Coutures JP (1994) Residual carbon detection in barium-titanate ceramics by nuclear-reaction technique. J Eur Ceram Soc 3:215–219

Ramos E, Lackey JS, Barnes J, Fulton A (2020) Remnants and rates of metamorphic decarbonation in Continental Arcs. GSAT 30:4–10. https://doi.org/10.1130/GSATG432A.1

Regnier P, Lasaga A, Berner R, Han O, Zilm K (1994) Mechanism of CO23– substitution in carbonate-fluorapatite: evidence from FTIR spectroscopy, 13C NMR, and quantum mechanical calculations. Am Miner 79:809–818

Riker J, Humphreys MCS, Brooker RA, Hoog JCMD (2018) First measurements of OH-C exchange and temperature-dependent partitioning of OH and halogens in the system apatite–silicate melt. Am Miner 103:260–270. https://doi.org/10.2138/am-2018-6187CCBY

Rubatto D, Hermann J, Berger A, Engi M (2009) Protracted fluid-induced melting during Barrovian metamorphism in the Central Alps. Contrib Miner Petrol 158:703–722. https://doi.org/10.1007/s00410-009-0406-5

Santos RV, Clayton RN (1995) The carbonate content in high-temperature apatite: An analytical method applied to apatite from the Jacupiranga alkaline complex. Am Miner 80:336–344

Skelton A (2011) Flux rates for water and carbon during greenschist facies metamorphism. Geology 39:43–46. https://doi.org/10.1130/G31328.1

Spear FS, Pyle JM (2002) Apatite, monazite, and xenotime in Metamorphic Rocks. Rev Min Geochem 48:293–335. https://doi.org/10.2138/rmg.2002.48.7

Stewart EM, Ague JJ (2018) Infiltration-driven metamorphism, New England, USA: Regional CO2 fluxes and implications for Devonian climate and extinctions. Earth Planet Sci Lett 489:123–134. https://doi.org/10.1016/j.epsl.2018.02.028

Stewart EM, Ague JJ (2020) Pervasive subduction zone devolatilization recycles CO 2 into the forearc. Nat Commun 11:6220. https://doi.org/10.1038/s41467-020-19993-2

Stock MJ, Humphreys MCS, Smith VC et al (2018) Tracking volatile behaviour in sub-volcanic plumbing systems using apatite and glass: insights into pre-eruptive processes at Campi Flegrei, Italy. J Petrol 59:2463–2492. https://doi.org/10.1093/petrology/egy020

Stormer J, Pierson ML, Tacker RC (1993) Variation of F and Cl X-ray intensity due to anisotropic diffusion in apatite. Am Miner 78:641–648

Tacker RC (2004) Hydroxyl ordering in igneous apatite. Am Miner 89:1411–1421. https://doi.org/10.2138/am-2004-1008

Tacker RC (2008) Carbonate in igneous and metamorphic fluorapatite: two type A and two type B substitutions. Am Miner 93:168–176. https://doi.org/10.2138/am.2008.2551

Tirira J, Frontier JP, Trocellier P, Trouslard P (1991) Development of a simulation algorithm for energy spectra of elastic recoil spectrometry. Nucl Inst Methods Phys Res B 54(328–333):1991

Todd CS, Engi M (1997) Metamorphic field gradients in the Central Alps. J Metam Geol 15:513–530. https://doi.org/10.1111/j.1525-1314.1997.00038.x

Tollan P, Hermann J (2019) Arc magmas oxidized by water dissociation and hydrogen incorporation in orthopyroxene. Nat Geosci 12:667–671. https://doi.org/10.1038/s41561-019-0411-x

Wang YQ (2004) Hydrogen standards in elastic recoil detection analysis. Nucl Instrum Methods Phys Res B 219(1):115–124

Wang Y, Nastasi M (eds) (2009) Handbook of modern ion beam materials analysis, 2nd edn. Materials Research Society, Washington, D.C

Wang KL, Zhang Y, Naab FU (2011) Calibration for IR measurements of OH in apatite. Am Miner 96(8–9):1392–1397. https://doi.org/10.2138/am.2011.3756

Weinberg RF, Hasalová P (2015) Water-fluxed melting of the continental crust: a review. Lithos 212–215:158–188. https://doi.org/10.1016/j.lithos.2014.08.021

Williams-Jones AE, Heinrich CA (2005) 100th Anniversary special paper: vapor transport of metals and the formation of magmatic-hydrothermal ore deposits. Econ Geol 100:1287–1312

Yang Q, Xia X-P, Zhang L et al (2020) Oxygen isotope homogeneity assessment for apatite U–Th–Pb geochronology reference materials. Surf Interface Anal 52:197–213. https://doi.org/10.1002/sia.6717

Zhu C, Sverjensky DA (1991) Partitioning of F-Cl-OH between minerals in hydrothermal fluids. Geochim Cosmochim Acta 55:1837–1858

Publisher's Note Springer Nature remains neutral with regard to jurisdictional claims in published maps and institutional affiliations.